ABSTRACT

Title of dissertation: QUANTUM THERMALIZATION AND
LOCALIZATION IN A TRAPPED ION
QUANTUM SIMULATOR

Jacob Smith, Doctor of Philosophy, 2016

Dissertation directed by: Professor Christopher Monroe
Joint Quantum Institute,
University of Maryland Department of Physics and
National Institute of Standards and Technology

When a system thermalizes it loses all memory of its initial conditions. Even within a closed quantum system, subsystems usually thermalize using the rest of the system as a heat bath. Exceptions to quantum thermalization have been observed, but typically require inherent symmetries or noninteracting particles in the presence of static disorder. The prediction of many-body localization (MBL), in which disordered quantum systems can fail to thermalize despite strong interactions and high excitation energy, was therefore surprising and has attracted considerable theoretical attention. We experimentally generate MBL states by applying an Ising Hamiltonian with long-range interactions and programmably random disorder to ten spins initialized far from equilibrium with respect to the Hamiltonian. Using experimental and numerical methods we observe the essential signatures of MBL: initial state memory retention, Poissonian distributed many-body energy level spacings, and evidence of long-time entanglement growth. Our platform can be scaled

to more spins, where detailed modeling of MBL becomes impossible.

QUANTUM THERMALIZATION AND LOCALIZATION IN A TRAPPED ION QUANTUM SIMULATOR

by

Jacob Smith

Dissertation submitted to the Faculty of the Graduate School of the
University of Maryland, College Park in partial fulfillment
of the requirements for the degree of
Doctor of Philosophy
2016

Advisory Committee:
Professor Christopher Monroe, Chair/Advisor
Professor Charles Clark
Professor Jacob Taylor
Professor Vladimir Manucharyan
Professor Edo Waks

Dedication

To my parents

Acknowledgments

Grad school was really tough for me and a lot of people helped me along the way. Instead of going through a long list of people to thank and risk omiting someone, I would just like to say that although I haven't always made my graditude known, I'm greatly indebted to all of these people.

Table of Contents

List of Figures

List of Abbreviations

AOM	Acousto-optic modulator
(P)BS	(Polarizing) beam splitter
CW	Continuous wave
EOM	Electro-optic modulator
HW	Half-wave plate
HD	Hamming distance
h.c.	Hermitian conjugate
ICCD	Intensified charge coupled device
MBL	Many-body localization
PID	Proportional integral derivative
QFI	Quantum Fisher information
RF	Radio frequency

Chapter 1:   Introduction

1.1   Cold Atoms for Quantum Simulation

When a system thermalizes it loses all memory of its initial conditions. Even within a closed quantum system, subsystems can thermalize using the rest of the system as a heat bath. However, it is still an open question whether a quantum system will thermalize [1–12]. In the case that it can thermalize the dynamics leading to thermalization are, in general, not well understood and can be non-trivial [13–16]. Determining if a quantum system can thermalize is an important question because in a thermal state one can use statistical mechanics to describes the system's dynamics with limited knowledge [17].

Cold atom systems have distinguished themselves as a leading platform for quantum simulation [18, 19]. They have been used to investigate thermalization in closed quantum systems [4, 7, 8, 10–12, 14, 16, 17, 20–25] with a recent simulation in a neutral atom system studying features of many-body localized (MBL) that cannot be simulated with classical numerics [22]. In particular, cold atom quantum simulators have been used to study the absence of thermalization in integrable systems [4] and in the cases of Anderson localization [7, 8, 20] and MBL [10–12, 21–23], and have studied non-trivial dynamics before a system thermalizes [14, 16, 17, 25].

Trapped ions [11, 25–38] bring the unique feature of tunable long-range interactions [26, 39, 40] to the quantum simulation table. In the context of MBL this allows study of the open theoretical question of what ranges of interactions support an MBL phase [41–44]. I will discuss data where we scan the range of the interaction over a set of parameters where some predict many-body delocalization [43]. Moreover, trapped ions have site-specific readout, which in the case of studying thermalization in closed quantum systems allows for one to determine if subsystems down to the single-spin level can use the rest of the system as an effective heat bath.

1.2   Outline of Thesis

While I have been in the lab we have performed studies of adiabatic quantum simulation [32–34], excited state dynamics [35, 37], quantum simulations in spin-1 systems [38], and the dynamics leading to thermalization [25]. However, this thesis will only discuss our investigations of MBL [11].

Chapter 2 discusses the atom laser interactions that we use to perform quantum simulations. In particular, I present a detailed discussion of a fourth-order Stark Shift [45] that we use to implement programmable random disorder and prepare arbitrary initial states in order to study MBL. Moreover, I discuss inhomogeneities that arise in the Ising couplings due to the normal mode structure.

Chapter 3 gives an overview of the experimental apparatus and then jumps into the details of a couple components of the setup that are new or were not covered in previous theses on the project [46–49]. One of these topic is the astigmatism that

is present in the laser beams that are used to drive the spin-spin interactions in our system. Another is the individual addressing beam path. Also, I will discuss in detail our investigations of the stability of the trapping radio frequency (RF) potential and our subsequent attempts to lock it [50].

Chapter 4 describes our experimental investigation of MBL [11]. We observe the essential features of MBL: initial state memory retention, Poissonian distributed energy level spacings, and evidence of long-time entanglement growth. This chapter contains an in depth discussion of the evidence of long-time entanglement growth which was witnessed using quantum Fisher information (QFI). This discussion makes qualitative connections between growth in the QFI and growth in the half-chain entanglement entropy which is a more direct measure of entanglement.

Chapter 2: Atom-Laser Interaction

2.1 Overview

In this chapter I will present the atom-laser interactions that are central to the quantum simulations discussed in this thesis. Since previous theses [46,48] have provided detailed derivations of the effective Ising interaction using the Magnus expansion and effective Hamiltonian theory [47,51] I will only give a high level overview of the derivation of the effective spin-spin interaction using the Magnus expansion. However, I will present a detailed derivation of the fourth-order Stark shift that has enabled [45] the initialization of arbitrary product states and the application of site-specific transverse magnetic field terms in our effective Hamiltonians. At the end, I discuss the way the normal mode stucture affects the effective spin-spin coupling profile, in particular, I will discuss the presence of an inhomogeneity in the nearest neighbor coupling across the spin chain.

2.2 Stark Shifts and Stimulated Raman Transitions

We will start by considering the simplified model of two CW beams with frequencies, ω_0 and ω_1, interacting with a three-level system schematically represented
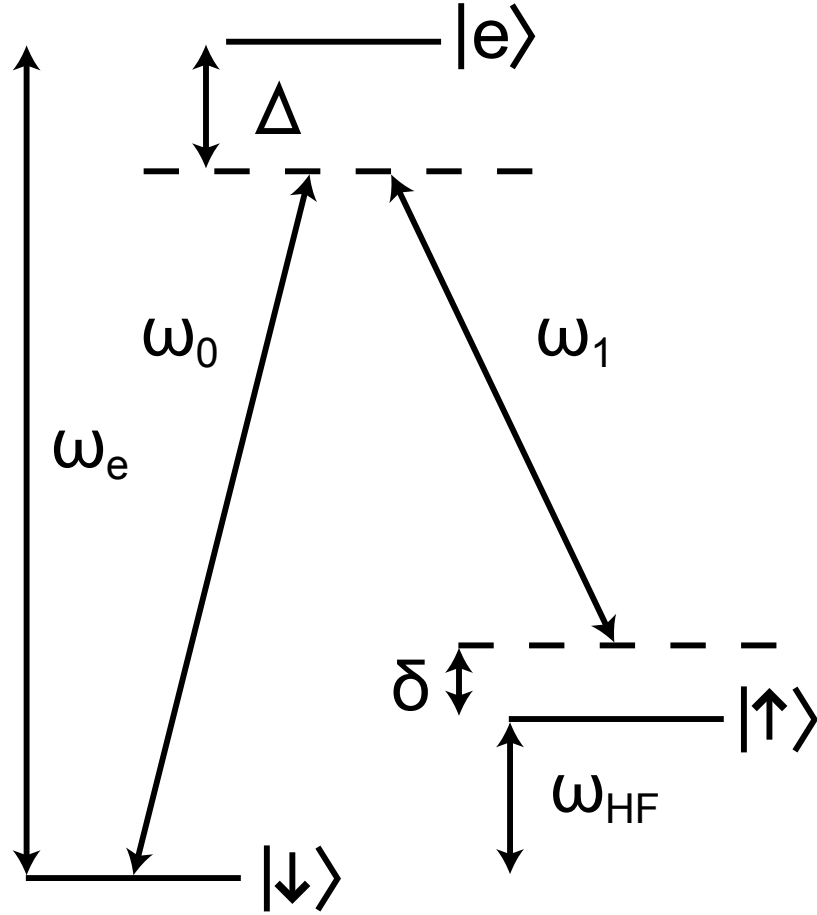
Figure 2.1: **Schematic Diagram of Three Level System.** Schematic diagram of a three level system addressed by two laser beams at different frequencies. After performing transformations to a rotating frame where the Hamiltonian is stationary, one can treat the coupling terms between states as a perturbation to the diagonal terms of the Hamiltonian using time-independent perturbation theory. Although the second-order Stark shift for the experimental parameters is relatively small because of cancellations of the second-order Stark shifts from the $^2P_{1/2}$ and $^3P_{3/2}$ levels, the fourth-order energy correction is about 1000 times larger and can be used to prepare arbitrary initial states and apply disordered effective field terms.

in Figure 2.1. The bare Hamiltonian is:

$$H_0 = \omega_e |e\rangle \langle e| + \omega_{HF} |\uparrow\rangle \langle\uparrow|, \tag{2.1}$$

Assuming that $\omega_{HF} \ll \omega_e, \omega_1, \omega_0$ and thus $|\uparrow\rangle$ and $|\downarrow\rangle$ cannot be coupled with a single photon. The two CW electric fields can be written as:

$$E(\mathbf{r}, t) = \sum_{i=0}^{1} \frac{E_i}{2} (e^{i(\mathbf{k}_i \cdot \mathbf{r} - \omega_i t - \phi_i)} + e^{-i(\mathbf{k}_i \cdot \mathbf{r} - \omega_i t - \phi_i)}) \hat{\epsilon}_i, \tag{2.2}$$

where $\mathbf{k}_i$ is the laser wavevector, ϕ_i is the laser phase, E_i is the electric field strength, and $\hat{\epsilon}_i =$ is the polarization in the frame of the ion with $|\epsilon_i^-|^2 + |\epsilon_i^0|^2 + |\epsilon_i^+|^2 = 1$. We will ignore the phase and the wavevector for this derivation of the Stark shifts. The laser-ion interaction for dipole allowed transitions is given by:

$$\begin{aligned} H_{int} &= -\vec{\mu} \cdot \vec{E} \\ &= (\frac{\Gamma_0}{2} |\downarrow\rangle \langle e| + \frac{\Gamma_0}{2} |\uparrow\rangle \langle e| + h.c.)(e^{i\omega_0 t} + e^{-i\omega_0 t}) \\ &\quad + (\frac{\Gamma_1}{2} |\downarrow\rangle \langle e| + \frac{\Gamma_1}{2} |\uparrow\rangle \langle e| + h.c.)(e^{i\omega_1 t} + e^{-i\omega_1 t}), \end{aligned} \tag{2.3}$$

with $\Gamma_i = g_i C(\hat{\epsilon}_i)$, where $g_i^2 = \frac{\gamma^2 \bar{I}_i}{2I_0}$ is the resonant $S \longrightarrow P$ Rabi frequency with time-averaged beam intensity, $\bar{I}_i$, and saturation intensity of the transition, I_0. $C(\hat{\epsilon}_i)$ is the dipole matrix coupling element for a given polarization. The relevant coupling coefficients for ^{171}Yb$^+$ can be seen in Tables 2.1 and 2.2 and a detailed description of how they can be calculated using the Wigner-Eckart theorem [52, 53] is given in [54]. We will now transform the full Hamiltonian, $H = H_0 + H_{int}$ into a rotating

6

frame given by the unitary transformation $U|e\rangle = e^{-i\omega_0 t}|e\rangle$. The Hamiltonian in the rotating frame is given by:

$$
\begin{aligned}
H' &= U^\dagger H U - i U^\dagger \frac{\partial U}{\partial t} \\
&= U^\dagger (H'_0 + H'_{int}) U - \omega_0 |e\rangle\langle e|.
\end{aligned}
\tag{2.4}
$$

Thus

$$
\begin{aligned}
H' =\, &\omega_{HF} |\uparrow\rangle \langle\uparrow| + \Delta |e\rangle\langle e| \\
&+ (\frac{\Gamma_0}{2} |\downarrow\rangle \langle e| e^{i\omega_0} + \frac{\Gamma_0}{2} |\uparrow\rangle \langle e| e^{i\omega_0} + h.c.)(e^{i\omega_0 t} + e^{-i\omega_0 t}) \\
&+ (\frac{\Gamma_1}{2} |\downarrow\rangle \langle e| e^{i\omega_0} + \frac{\Gamma_1}{2} |\uparrow\rangle \langle e| e^{i\omega_0} + h.c.)(e^{i\omega_1 t} + e^{-i\omega_1 t}).
\end{aligned}
\tag{2.5}
$$

Making a rotating wave approximation where one does not consider all terms rotating at $2\omega_i$, leaves:

$$
\begin{aligned}
H^{`} =\, &\omega_{HF} |1\rangle\langle 1| + \Delta |e\rangle\langle e| \\
&+ (\frac{\Gamma_0}{2} |\downarrow\rangle \langle e| + \frac{\Gamma_0}{2} |\uparrow\rangle \langle e| + h.c.) \\
&+ (\frac{\Gamma_1}{2} |\downarrow\rangle \langle e| e^{i(\omega_0 - \omega_1)t} + \frac{\Gamma_1}{2} |\uparrow\rangle \langle e| e^{i(\omega_0 - \omega_1)t} + h.c.).
\end{aligned}
\tag{2.6}
$$

Applying a second unitary transformation of $U |\uparrow\rangle = e^{-i(\omega_0 - \omega_1)t} |\uparrow\rangle$ and another rotating wave approximation discarding terms oscillating at $\omega_0 - \omega_1$, leaves:

$$
H'' = \delta |\uparrow\rangle \langle\uparrow| + \Delta |e\rangle\langle e| + \frac{\Gamma_0}{2} |\downarrow\rangle \langle e| + \frac{\Gamma_0}{2} |e\rangle \langle\downarrow| + \frac{\Gamma_1}{2} |\uparrow\rangle \langle e| + \frac{\Gamma_1}{2} |e\rangle \langle\uparrow|.
\tag{2.7}
$$

Where $\delta = (\omega_{HF} - (\omega_0 - \omega_1))$. Now that we have a stationary Hamiltonian we will apply non-degenerate, time-independent perturbation theory with $H_0 = \delta |{\uparrow}\rangle\langle{\uparrow}| + \Delta|e\rangle\langle e|$ and treat the off-diagonal terms as a perturbation, $V = \frac{\Gamma_0}{2}|{\downarrow}\rangle\langle e| + \frac{\Gamma_0}{2}|e\rangle\langle{\downarrow}| + \frac{\Gamma_1}{2}|{\uparrow}\rangle\langle e| + \frac{\Gamma_1}{2}|e\rangle\langle{\uparrow}|$. Since, the dipole operator cannot couple a spherically symmetric level to itself the first-order light shift is zero. The nonvanishing second-order correction to the energy is:

$$\Delta E_n^{(2)} = \sum_{m\neq n} \frac{|\langle n|V|m\rangle|^2}{E_n^{(0)} - E_m^{(0)}}. \tag{2.8}$$

Applying (2.8) to $|{\downarrow}\rangle$:

$$\begin{aligned}
\Delta E_{|{\downarrow}\rangle}^{(2)} &= \sum_{m\neq n} \frac{|\langle{\downarrow}|V|e\rangle|^2}{E_{|{\downarrow}\rangle}^{(0)} - E_e^{(0)}} \\
&= \frac{|\Gamma_0|^2}{4(0-\Delta)} = -\frac{|\Gamma_0|^2}{4\Delta}.
\end{aligned} \tag{2.9}$$

Applying (2.8) to $|{\uparrow}\rangle$ with $\Delta \gg \delta$:

$$\begin{aligned}
\Delta E_{|{\uparrow}\rangle}^{(2)} &= \sum_{m\neq n} \frac{|\langle{\uparrow}|V|e\rangle|^2}{E_{|{\uparrow}\rangle}^{(0)} - E_e^{(0)}} \\
&= \frac{|\Gamma_1|^2}{4(\delta-\Delta)} \approx -\frac{|\Gamma_1|^2}{4\Delta}.
\end{aligned} \tag{2.10}$$

Thus, the differential stark shift on these two levels is:

$$\Delta E_{\text{diff}|{\downarrow}\rangle|{\uparrow}\rangle}^{(2)} = \Delta E_{|{\uparrow}\rangle}^{(2)} - \Delta E_{|{\downarrow}\rangle}^{(2)} = \frac{|\Gamma_1|^2 - |\Gamma_0|^2}{4\Delta}. \tag{2.11}$$

$\overline{F=2,m_F=-2}$ $\overline{F=2,m_F=-1}$ $\overline{F=2,m_F=0}$ $\overline{F=2,m_F=1}$ $\omega_{3/2}$ $\overline{F=2,m_F=2}$

$^3P_{3/2}$ $\overline{F=1,m_F=-1}$ $\overline{F=1,m_F=0}$ $\overline{F=1,m_F=1}$

Δ' ω_{FS}

Δ

$^2P_{1/2}$ $\overline{F=1,m_F=-1}$ $\overline{F=1,m_F=0}$ $\overline{F=1,m_F=1}$ $\omega_{1/2}$ $\underline{F=0,m_F=0}$

$^2S_{1/2}$ $\overline{F=1,m_F=-1}\,|-\rangle$ $\overline{F=1,m_F=0}\,|\uparrow\rangle$ $\overline{F=1,m_F=1}\,|+\rangle$ ω_{HF} $\underline{F=0,m_F=0}\,|\downarrow\rangle$
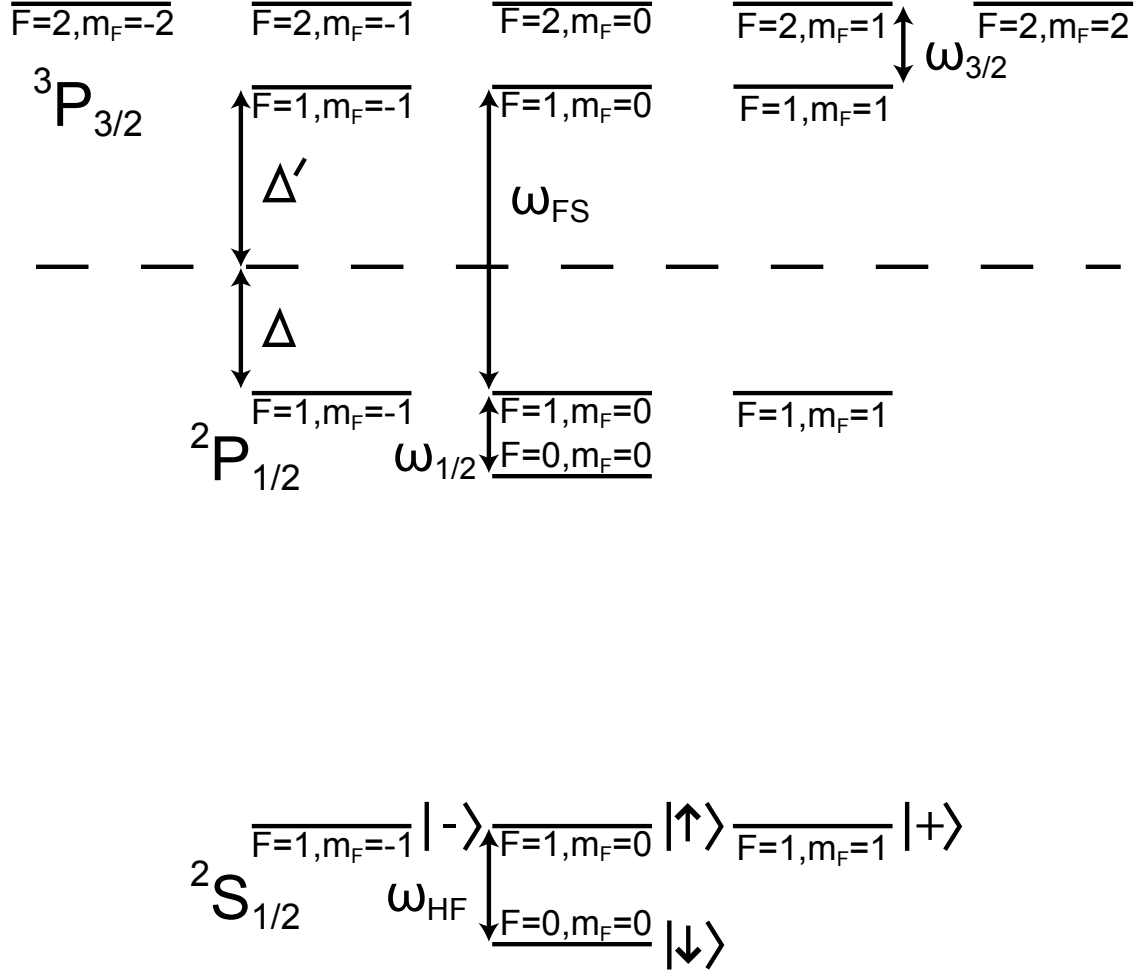
Figure 2.2: **Yb Raman Level Diagram.** Schematic diagram of all of the states in the $^2S_{1/2}$, $^2P_{1/2}$, and $^3P_{3/2}$ manifolds. All but the $|^3P_{3/2}, F = 2, m_F = \pm2\rangle$ states have dipole allowed transitions that could affect the Stark shift of the $|\downarrow\rangle$ and $|\uparrow\rangle$ levels (provided non-zero coupling coefficients between the states).

Applying (2.8) to the real $^{171}\text{Yb}^+$ system (excluding a $^3[3/2]_{3/2}$ bracket state which is ≈ 50 THz above the $^2P_{1/2}$ line and only changes the second order shift by 10% [45]) as seen in Figure 2.2 and using the coupling coefficients in Tables 2.1 and 2.2, Gives a Stark shift on the qubit states and Zeeman levels of:

$$
\begin{aligned}
\Delta E_{|\downarrow\rangle}^{(2)} =& \frac{g_0^2}{12\Delta} + \frac{g_1^2}{12(\Delta - \omega_{HF})} - \frac{g_0^2}{6\Delta'} - \frac{g_1^2}{6(\Delta' + \omega_{HF})}, \\
\Delta E_{|\uparrow\rangle}^{(2)} =& \frac{g_0^2((\epsilon_0^+)^2 + (\epsilon_0^-)^2)}{12(\Delta + \omega_{HF})} + \frac{g_0^2(\epsilon_0^\pi)^2}{12(\Delta + \omega_{HF} + \omega_{1/2})} + \frac{g_1^2((\epsilon_1^+)^2 + (\epsilon_1^-)^2)}{12\Delta} + \frac{g_1^2(\epsilon_1^\pi)^2}{12(\Delta + \omega_{1/2})} \\
& - \frac{g_0^2((\epsilon_0^-)^2 + (\epsilon_0^+)^2)}{24(\Delta' - \omega_{HF})} - \frac{g_0^2(3 + (\epsilon_0^\pi)^2)}{24(\Delta' - \omega_{HF} + \omega_{3/2})} - \frac{g_1^2((\epsilon_1^-)^2 + (\epsilon_1^+)^2)}{24(\omega_{FS} - \Delta)} - \frac{g_1^2(3 + (\epsilon_1^\pi)^2)}{24(\Delta' + \omega_{3/2})}, \\
\Delta E_{|\pm\rangle}^{(2)} =& \frac{g_0^2((\epsilon_0^\pi)^2 + (\epsilon_0^\pm)^2)}{12(\Delta + \omega_{HF})} + \frac{g_0^2(\epsilon_0^\pm)^2}{12(\Delta + \omega_{HF} + \omega_{1/2})} + \frac{g_1^2((\epsilon_1^\pi)^2 + (\epsilon_1^\pm)^2)}{12\Delta} + \frac{g_1^2(\epsilon_1^\pm)^2}{12(\Delta + \omega_{1/2})} \\
& - \frac{g_0^2(1 + 2(\epsilon_0^\pi)^2 + 5(\epsilon_0^\pm)^2)}{24(\Delta' - \omega_{HF} + \omega_{3/2})} - \frac{g_0^2((\epsilon_0^\pi)^2 + (\epsilon_0^\pm)^2)}{24(\Delta' - \omega_{HF})} - \frac{g_1^2(1 + 2(\epsilon_1^\pi)^2 + 5(\epsilon_1^\pm)^2)}{24(\Delta' + \omega_{3/2})} \\
& - \frac{g_1^2((\epsilon_1^\pi)^2 + (\epsilon_1^\pm)^2)}{24\Delta'}.
\end{aligned}
$$

(2.12)

Writing the frequencies normalized by the fine-structure splitting ω_{FS}, $\tilde\Delta = \Delta/\omega_{FS} \approx 0.339$, $\tilde\Delta' = \Delta'/\omega_{FS} \approx 0.661$, $\tilde\omega_{HF} = \omega_{HF}/\omega_{FS} \approx 1.26 \times 10^{-4}$, $\tilde\omega_{1/2} = \omega_{1/2}/\omega_{FS} \approx 2 \times 10^{-5}$, $\tilde\omega_{3/2} = \omega_{3/2}/\omega_{fs} \approx 2 \times 10^{-5}$ and expanding to lowest-order in $\tilde\omega_{HF}$, $\tilde\omega_{1/2}$, and $\tilde\omega_{3/2}$ yields a differential AC stark shift between $|\downarrow\rangle$ and $|\uparrow\rangle$ of:

$$
\begin{aligned}
\Delta E_{\text{diff}|\downarrow\rangle|\uparrow\rangle}^{(2)} = & -\frac{g_0^2 + g_1^2}{12\omega_{FS}}\left(\frac{\tilde\omega_{HF}}{\tilde\Delta^2}\right) - \frac{g_0^2(\epsilon_0^\pi)^2 + g_1^2(\epsilon_1^\pi)^2}{12\omega_{FS}}\left(\frac{\tilde\omega_{1/2}}{\tilde\Delta^2}\right) \\
& -\frac{g_0^2 + g_1^2}{6\omega_{FS}}\left(\frac{\tilde\omega_{HF}}{\tilde\Delta'^2}\right) + \frac{g_0^2(\epsilon_0^\pi)^2 + g_1^2(\epsilon_1^\pi)^2}{24\omega_{FS}}\left(\frac{\tilde\omega_{3/2}}{\tilde\Delta'^2}\right).
\end{aligned}
$$

(2.13)

If one ignores the hyperfine splitting of the P manifold (it has small effect of order $\approx 10^{-5}$) then one finds simpler expressions for the second-order Stark shifts on the $|\downarrow\rangle$ and $|\uparrow\rangle$ states:

$$
\begin{aligned}
\Delta E^{(2)}_{|\downarrow\rangle} &= \frac{g_0^2}{12}\left(\frac{1}{\Delta} - \frac{2}{\omega_{FS} - \Delta}\right), \\
\Delta E^{(2)}_{|\uparrow\rangle} &= \frac{g_0^2}{12}\left(\frac{1}{\Delta + \omega_{HF}} - \frac{2}{\omega_{FS} - (\Delta + \omega_{HF})}\right).
\end{aligned}
\tag{2.14}
$$

For an individual addressing beam with 20 mW of time-average power focused tightly to a 3 μm waist, we find $\Delta E^{(2)}_{\text{diff}|\downarrow\rangle|\uparrow\rangle} = -1.5$ kHz. This is a small shift because of the cancellations of the Stark shifts from the $^2P_{1/2}$ and $^3P_{3/2}$ levels. Thus to achieve sufficiently large Stark shifts from the individual addressing beam to use for arbitrary product state preparation and for the application of a random disordered field one must look to higher-order energy corrections.

Expanding the differential AC Stark shift between $|\downarrow\rangle$ and the Zeeman states, $|\pm\rangle$, to lowest-order in $\tilde{\omega}_{HF}$, $\tilde{\omega}_{1/2}$, and $\tilde{\omega}_{3/2}$ gives:

$$
\begin{aligned}
\Delta E^{(2)}_{\text{diff}|\downarrow\rangle|\pm\rangle} = \mp \frac{g_0^2 c_0 + g_1^2 c_1}{12\omega_{FS}}\left(\frac{1}{\tilde{\Delta}} + \frac{1}{\tilde{\Delta}'}\right) - \frac{g_0^2 + g_1^2}{12\omega_{FS}}\left(\frac{\tilde{\omega}_{HF}}{\tilde{\Delta}^2} + \frac{2\tilde{\omega}_{HF}}{\tilde{\Delta}'^2}\right) \\
- \frac{g_0^2(\epsilon_0^\mp)^2 + g_1^2(\epsilon_1^\mp)^2}{12\omega_{FS}}\left(\frac{\omega_{1/2}}{\tilde{\Delta}^2}\right) - \frac{(g_0^2 + g_1^2)(3 + 3(\epsilon_0^\mp)^2 - 2(\epsilon_0^\pm)^2)}{24\omega_{FS}}\left(\frac{\tilde{\omega}_{3/2}}{\tilde{\Delta}'^2}\right).
\end{aligned}
\tag{2.15}
$$

With $c_i = (\epsilon_i^+)^2 - (\epsilon_i^-)^2$ a measure of the circular polarization of the ith beam.

The next non-zero correction to the energy is given by a fourth-order perturbation. Using the notation $V_{ab} = \langle a|V|b\rangle$ and $E_{ab} = E_a^{(0)} - E_b^{(0)}$ this fourth-order

shift can be written as:

$$\Delta E_n^{(4)} = \sum_{k,l,m \neq n} \frac{V_{nm}V_{ml}V_{lk}V_{kn}}{E_{nm}E_{nl}E_{nk}} - \Delta E_n^{(2)} \frac{|V_{nm}|^2}{E_{nm}^2} - 2V_{nn} \frac{V_{nm}V_{ml}V_{ln}}{E_{nl}^2 E_{nm}} + V_{nn}^2 \frac{|V_{nm}|^2}{E_{nm}^3}. \quad (2.16)$$

Using $V_{nn} = 0$ and that $m, l, k \neq n$ gives a shift for $|\downarrow\rangle$ and $|\uparrow\rangle$:

$$
\begin{aligned}
\Delta E_{|\downarrow\rangle}^{(4)} &= \frac{V_{|\downarrow\rangle e}V_{e|\uparrow\rangle}V_{|\uparrow\rangle e}V_{e|\downarrow\rangle}}{E_{|\downarrow\rangle e}E_{|\downarrow\rangle|\uparrow\rangle}E_{|\downarrow\rangle e}} - \Delta E_{|\downarrow\rangle}^2 \frac{|V_{|\downarrow\rangle e}|^2}{E_{|\downarrow\rangle e}^{(2)}} \\
&= \frac{|\Gamma_0|^2|\Gamma_1|^2}{16(0-\Delta)(0-\delta)(0-\Delta)} - \left(\frac{-|\Gamma_0|^2}{4\Delta} \right) \frac{\Gamma_0^2}{4\Delta^2} \\
&= -\frac{|\Gamma_0|^2|\Gamma_1|^2}{16\Delta^2\delta} + \frac{|\Gamma_0|^4}{16\Delta^3}, \\
\Delta E_{|\uparrow\rangle}^{(4)} &= \frac{V_{|\uparrow\rangle e}V_{e|\downarrow\rangle}V_{|\downarrow\rangle e}V_{e|\uparrow\rangle}}{E_{|\uparrow\rangle e}E_{|\uparrow\rangle|\downarrow\rangle}E_{|\uparrow\rangle e}} - \Delta E_{|\uparrow\rangle}^{(2)} \frac{|V_{|\uparrow\rangle e}|^2}{E_{|\uparrow\rangle e}^2} \\
&= \frac{|\Gamma_1|^2|\Gamma_0|^2}{16(\delta-\Delta)(\delta-0)(\delta-\Delta)} - \left(\frac{-|\Gamma_1|^2}{4\Delta} \right) \frac{|\Gamma_1|^2}{4(\delta-\Delta)^2} \\
&\approx \frac{|\Gamma_1|^2|\Gamma_0|^2}{16\Delta^2\delta} + \frac{|\Gamma_1|^4}{16\Delta^3}.
\end{aligned}
\quad (2.17)
$$

Rewriting this in terms of the two-photon Rabi frequency $\Omega = \frac{\Gamma_0\Gamma_1}{2\Delta}$ and using the aforementioned assumption that $\delta \ll \Delta$ gives a fourth-order Stark shift of:

$$
\begin{aligned}
\Delta E_{|\downarrow\rangle}^{(4)} &= -\frac{|\Omega|^2}{4\delta}, \\
\Delta E_{|\uparrow\rangle}^{(4)} &= \frac{|\Omega|^2}{4\delta}.
\end{aligned}
\quad (2.18)
$$

As for the case with the second-order energy shift we will now apply this formula to ^{171}Yb$^+$ (once again excluding the contributions from the $^3[3/2]_{3/2}$ state). Thus the total fourth-order Stark shift is given by:

$$\Delta E_n^{(4)} = \sum_{a \neq n} \frac{\Omega_{n,a}^2}{4\delta_{n,a}}. \tag{2.19}$$

In the previous equation $\Omega_{n,a}$ is the two-photon Rabi frequency between $|n\rangle$ and $|a\rangle$, $\delta_{n,a} = \omega_a - (\omega_0 - \omega_1)$, and $\omega_a = E_a^{(0)} - E_n^{(0)}$. The necessary Rabi frequencies for this calculation are (once again ignoring the hyperfine structure of the excited states):

$$\begin{aligned}
\Omega_{|\downarrow\rangle,|\uparrow\rangle} &= (\epsilon_0^- \epsilon_1^- - \epsilon_0^+ \epsilon_1^+)\Omega_0, \\[4pt]
\Omega_{|\downarrow\rangle,|-\rangle} &= -(\epsilon_0^- \epsilon_1^\pi + \epsilon_0^\pi \epsilon_1^+)\Omega_0, \\[4pt]
\Omega_{|\downarrow\rangle,|+\rangle} &= (\epsilon_0^+ \epsilon_1^\pi + \epsilon_0^\pi \epsilon_1^-)\Omega_0, \\[4pt]
\Omega_{|\uparrow\rangle,|-\rangle} &= (\epsilon_0^- \epsilon_1^\pi + \epsilon_0^\pi \epsilon_1^+)\Omega_0, \\[4pt]
\Omega_{|\uparrow\rangle,|+\rangle} &= (\epsilon_0^+ \epsilon_1^\pi + \epsilon_0^\pi \epsilon_1^-)\Omega_0,
\end{aligned} \tag{2.20}$$

with $\Omega_0 = \frac{g_0^2}{6}(\frac{1}{\Delta} + \frac{1}{\omega_{FS} - \Delta})$. The maximum fourth-order light shift would occur for pure $\hat{\sigma}^\pm$ polarization, which has the largest Rabi frequency between the clock states, $\Omega_{|0\rangle,|1\rangle}$. However, due to the optical access in our experimental setup it is not possible to send in a beam with that polarization. Thus, the largest experimentally implementable fourth-order Stark shift occurs for $\hat{\epsilon} = \hat{\alpha} = 1/2\hat{\sigma}^- + 1/\sqrt{2}\hat{\pi} + 1/2\hat{\sigma}^+$. Due to the sign of the coupling coefficients, when $\hat{\epsilon} = \hat{\alpha}$ the fourth-order Stark shift on $|\uparrow\rangle$ from $|\pm\rangle$ cancel and $\Delta E_{|\uparrow\rangle}^{(4)} = 0$. For the two different polarizations discussed above, the differential fourth-order Stark shift between $|\downarrow\rangle$ and $|\uparrow\rangle$ is:

$$\Delta E^{(4)}_{\text{diff}|\downarrow\rangle|\uparrow\rangle} = \frac{\Omega_0^2}{2\delta_{|\downarrow\rangle,|\uparrow\rangle}} \text{ for } \hat{\epsilon} = \hat{\sigma}^{\pm},$$

$$\Delta E^{(4)}_{\text{diff}|\downarrow\rangle|\uparrow\rangle} = \frac{\Omega_0^2}{8} \left(\frac{1}{\delta_{|\downarrow\rangle,|-\rangle}} + \frac{1}{\delta_{|\downarrow\rangle,|+\rangle}} \right) \text{ for } \hat{\epsilon} = \hat{\alpha}. \tag{2.21}$$

Instead of considering just two applied frequencies, we will now discuss the experimental realization using a 355 nm pulsed laser beam with repetition rate, ω_{rep}, where all possible comb teeth pairs can contribute. One can write the two-photon Rabi frequency for two comb teeth, k_0 and k_1:

$$\Omega_n = \frac{g_{k_0}g_{k_1}}{2\Delta} \approx \text{sech}(\frac{n\omega_{rep}}{2}), \tag{2.22}$$

where $k_1 - k_0 = n$ and under the assumption the pulse bandwidth is significantly greater than ω_{HF}. Define j such that $|\omega_a - 2\pi j\omega_{rep}|$ is minimized and plug (2.22) into (2.19):

$$\Delta E_n^{(4)} = \sum_{a\neq n} \frac{\Omega_{n,a}^2}{4} \sum_{k=-\infty}^{\infty} \frac{\text{sech}^2((j+k)\pi\omega_{rep}\tau)}{\delta_{n,a} - k(2\pi\omega_{rep})}$$

$$= \sum_{a\neq n} C_{n,a} \frac{\Omega_{n,a}^2}{4\delta_{n,a}}, \tag{2.23}$$

with $\delta_{n,a} = \omega_a - j(2\pi\omega_{rep})$ and:

$$C_{n,a} = \sum_{k=-\infty}^{\infty} \frac{\text{sech}^2((j+k)\pi\omega_{rep}\tau)}{1 - \left(\frac{2\pi k\omega_{rep}}{\delta n,a}\right)}. \tag{2.24}$$

Only a few of the closest beatnotes contribute to the Stark shift as the denominator in (2.24) increases quickly. In addition, for ω_{rep} much greater than the Zeeman splitting of the $F = 1$ levels of the $^2S_{1/2}$ manifold, $\Delta E^4_{|\uparrow\rangle} = 0$. Now the differential fourth-order Stark shift can be written:

$$
\begin{aligned}
\Delta E^4_{\text{diff}|\downarrow\rangle|\uparrow\rangle} &= C_{|\downarrow\rangle,|\uparrow\rangle} \frac{\Omega_0^2}{2\delta_{|\downarrow\rangle,|\uparrow\rangle}} \text{for } \hat{\epsilon} = \hat{\sigma}_{\pm}, \\
\Delta E^4_{\text{diff}|\downarrow\rangle|\uparrow\rangle} &= \frac{\Omega_0^2}{8} \left(\frac{C_{|\downarrow\rangle,|-\rangle}}{\delta_{|\downarrow\rangle,|-\rangle}} + \frac{C_{|\downarrow\rangle,|+\rangle}}{\delta_{|\downarrow\rangle,|+\rangle}} \right) \text{for } \hat{\epsilon} = \alpha.
\end{aligned}
\tag{2.25}
$$

Using the same experimentally realistic parameters as above for calculating the second order shift of a time-averaged power of 20 mW focused down to 3 μm, and the laser parameters of $\omega_{rep}/2\pi = 120$ MHz, a pulse duration of $\tau \approx 14$ ps, and a bandwidth of about 70 GHz the fourth-order energy shift between $|\downarrow\rangle$ and $|\uparrow\rangle$ is:

$$
\begin{aligned}
\Delta E^{(4)}_{\text{diff}|\downarrow\rangle|\uparrow\rangle} &= 247 \text{ kHz for } \hat{\epsilon} = \hat{\sigma}^{\pm}, \\
\Delta E^{(4)}_{\text{diff}|\downarrow\rangle|\uparrow\rangle} &= 137 \text{ kHz for } \hat{\epsilon} = \hat{\alpha}.
\end{aligned}
\tag{2.26}
$$

The fourth-order Stark shift is about 100 times larger than the second-order Stark shift because of the cancellations of the second-order Stark shifts from the $^2P_{1/2}$ and $^3P_{3/2}$ levels allowing its use to prepare arbitrary initial product states and

	$^2S_{1/2}$: $F = 0, m_F = 0$	$^2S_{1/2}$: $F = 1, m_F = 0$
$^2P_{1/2}$: $F = 0, m_F = 0$	0	$1/\sqrt{3}$
$^2P_{1/2}$: $F = 1, m_F = -1$	$1/\sqrt{3}$	$1/\sqrt{3}$
$^2P_{1/2}$: $F = 1, m_F = 0$	$1/\sqrt{3}$	0
$^2P_{1/2}$: $F = 1, m_F = 1$	$1/\sqrt{3}$	$-1/\sqrt{3}$
$^3P_{3/2}$: $F = 1, m_F = -1$	$\sqrt{2/3}$	$-1/\sqrt{6}$
$^3P_{3/2}$: $F = 1, m_F = 0$	$\sqrt{2/3}$	0
$^3P_{3/2}$: $F = 1, m_F = 1$	$\sqrt{2/3}$	$1/\sqrt{6}$
$^3P_{3/2}$: $F = 2, m_F = -1$	0	$1/\sqrt{2}$
$^3P_{3/2}$: $F = 2, m_F = 0$	0	$\sqrt{2/3}$
$^3P_{3/2}$: $F = 2, m_F = 1$	0	$1/\sqrt{2}$

Table 2.1: Dipole coupling matrix element for different polarizations from $|^2S_{1/2}$: $F = 0, m_F = 0\rangle$ and $|^2S_{1/2}$: $F = 1, m_F = 0\rangle$ to excited P manifold.

apply disordered potentials to the ions.

2.3   Mølmer-Sørenson Interaction and Effective fields

For the discussion of the Mølmer-Sørenson interaction [39] I will start with the Hamiltonian for a laser field interacting with a two-level atom in a harmonic potential in an interaction picture with respect to the bare harmonic oscillator and atomic Hamiltonians [55]:

	$^2S_{1/2}$: $F = 1, m_F = -1$	$^2S_{1/2}$: $F = 1, m_F = 1$
$^2P_{1/2}$: $F = 0, m_F = 0$	$-1/\sqrt{3}$	$-1/\sqrt{3}$
$^2P_{1/2}$: $F = 1, m_F = -1$	$-1/\sqrt{3}$	0
$^2P_{1/2}$: $F = 1, m_F = 0$	$-1/\sqrt{3}$	$1/\sqrt{3}$
$^2P_{1/2}$: $F = 1, m_F = 1$	0	$1/\sqrt{3}$
$^3P_{3/2}$: $F = 1, m_F = -1$	$1/\sqrt{6}$	0
$^3P_{3/2}$: $F = 1, m_F = 0$	$1/\sqrt{6}$	$-1/\sqrt{6}$
$^3P_{3/2}$: $F = 1, m_F = 1$	0	$-1/\sqrt{6}$
$^3P_{3/2}$: $F = 2, m_F = -1$	$1/\sqrt{2}$	0
$^3P_{3/2}$: $F = 2, m_F = 0$	$1/\sqrt{6}$	$1/\sqrt{6}$
$^3P_{3/2}$: $F = 2, m_F = 1$	0	$1/\sqrt{2}$

Table 2.2: Dipole coupling matrix element for different polarizations from $|^2S_{1/2}$: $F = 0, m_F = -1\rangle$ and $|^2S_{1/2}$: $F = 1, m_F = 1\rangle$ to excited P manifold.

$$H = \frac{\Omega}{2} \left|\uparrow\right\rangle \left\langle\downarrow\right| \exp(i(\eta(ae^{-i\omega t} + a^\dagger e^{i\omega t}) - \delta t + \phi)) + h.c., \qquad (2.27)$$

Where $h = 1$, a and $a^\dagger$ are the raising and lowering operators of a harmonic oscillator with frequency ω, δ is the detuning from the atomic transition which in our case is ω_{hf}, $\eta = \Delta k x_0$ is the Lamb-Dicke parameter which is ≈ 0.16 in our setup, Δk is the wavevector difference and ϕ is the phase difference between the two photons used to drive the stimulated Raman transition, and $x_0 = \sqrt{\hbar/2m\omega}$ is the size of the harmonic oscillator ground state.

When the ion's motional wavepacket is much smaller than the wavelength or when $\eta^2(2\bar{n} + 1) \ll 1$, known as the Lamb-Dicke limit, then processes that change the motional state by more than one quanta are suppressed and one can use $e^{i\eta(ae^{-i\omega t} + a^\dagger e^{i\omega t})} \approx 1 + i\eta(ae^{-i\omega t} + a^\dagger e^{i\omega t})$. Then (2.27) can be approximated as:

$$H \approx \frac{\Omega}{2} \left|\uparrow\right\rangle \left\langle\downarrow\right| (1 + i\eta(ae^{-i\omega t} + a^\dagger e^{i\omega t}))e^{i(-\delta t + \phi)} + h.c., \qquad (2.28)$$

In the case of driving the atom on resonance, $\delta = 0$, one can disregard the phonon terms oscillating at $\pm\omega$, which gives a Hamiltonian of:

$$H_{carr} = \frac{\Omega}{2}(\left|\uparrow\right\rangle \left\langle\downarrow\right| e^{i\phi} + \left|\downarrow\right\rangle \left\langle\uparrow\right| e^{-i\phi}). \qquad (2.29)$$

We refer to this as driving a carrier transition. This allows manipulation of the

18

spin state without changing the motional state. We use carrier transitions for state initialization, reading out in the σ_x or σ_y basis, and to apply effective σ_x and σ_y fields in our simulated Hamiltonians. It is clear from (2.29) that with correct choice of phase the Hamiltonian simplifies to a σ_x or σ_y operator.

When $\delta = \pm\omega$ the stationary terms in the Hamiltonian are then the ones that change the motional state as well spin state. The Hamiltonian is then:

$$H_{rsb} = \frac{i\eta\Omega}{2}(\left|\uparrow\right\rangle \left\langle\downarrow\right| ae^{i\phi} - \left|\downarrow\right\rangle \left\langle\uparrow\right| a^{\dagger}e^{-i\phi}), \tag{2.30}$$

$$H_{bsb} = \frac{i\eta\Omega}{2}(\left|\uparrow\right\rangle \left\langle\downarrow\right| a^{\dagger}e^{i\phi} - \left|\downarrow\right\rangle \left\langle\uparrow\right| ae^{-i\phi}). \tag{2.31}$$

For $\delta = -\omega$, one gets (2.30), which is referred to as a red side band transition because the beatnote frequency is a harmonic oscillator frequency away from ω_{HF} and is equivalent to the Jaynes-Cummings Hamiltonian [56]. When the laser beatnote frequency is $\delta = \omega$ this is called the blue side band transition and is an anti-Jaynes-Cummings Hamiltonian.

In the case of the Mølmer-Sørenson interaction when both the red and blue sidebands are applied simultaneously one can write the Hamiltonian as [48]:

$$H_{MS} = \Omega\cos(\mu t + \phi_m)[\sigma^{\phi_s - \pi/2} + \eta\sigma^{\sigma_s}(ae^{-i\omega_t t} + a^{\dagger}e^{i\omega_t t})], \tag{2.32}$$

with:

$$\begin{aligned}
\phi_s &= \frac{\phi_r + \phi_b + \pi}{2}, \\
\phi_m &= \frac{\phi_r - \phi_b}{2}.
\end{aligned} \tag{2.33}$$

Generalizing this to many ions and many modes, choosing $\phi_r = 0$ and $\phi_b = \pi$ giving $\phi_s = \pi$ and $\phi_m = -\pi/2$, and disregarding the off-resonant coupling to the carrier transition gives:

$$H_{MS} = -\sum_{i,m} \eta_{i,m} \sin(\mu t) \sigma_i^x ((a_m e^{-i\omega_{t,m} t} + a_m^\dagger e^{i\omega_{t,m} t})). \tag{2.34}$$

The effective Ising interaction emerges from the Magnus expansion given by:

$$U(t) = T[e^{-i \int_0^t dt_1 H(t_1)}] = e^{\bar{\Omega}_1 + \bar{\Omega}_2 + \bar{\Omega}_3 + \cdots}, \tag{2.35}$$

Here, T is the time-ordering operator and the first three terms of the Magnus expansion are given by:

$$\begin{aligned}
\bar{\Omega}_1 &= -i \int_0^t dt_1 H(t_1), \\
\bar{\Omega}_2 &= -\frac{1}{2!} \int_0^t dt_1 \int_0^{t_1} dt_2 [H(t_1), H(t_2)], \\
\bar{\Omega}_3 &= \frac{i}{3!} \int_0^t dt_1 \int_0^{t_1} dt_2 \int_0^{t_2} dt_3 ([H(t_1), [H(t_2), H(t_3)]] + [H(t_3), [H(t_2), H(t_1)]]).
\end{aligned}$$

$$\tag{2.36}$$

Plugging (2.34) into the above equations gives the effective Ising interaction in the second order term emerging from the fact that the phonon raising and lowering operators for the same mode do not commute. When working in the far-detuned limit, $\eta_{i,m}\Omega_i \ll |\mu - \omega_m|$, which ensures that the normal modes are only virtually excited, allows one to ignore the spin-motion coupling terms, $\sigma_x^i a_m$ and $\sigma_x^i a_m^\dagger$ that emerge in the first order equation and one is left with:

$$U \approx \exp(-\sum_{i,j,m} \sigma_i^x \sigma_j^x \frac{i\eta_{i,m}\eta_{j,m}\Omega_i\Omega_j}{2(\mu^2 - \omega_m^2)}\omega_m t). \tag{2.37}$$

There are no higher order terms in the Magnus expansion as this second order term commutes with the base Hamiltonian.

Equation (2.37) is equivalent to the the time-evolution operator for a long-range Ising interaction:

$$H_{eff} = \sum_{i,j} J_{i,j}\sigma_i^x \sigma_j^x, \tag{2.38}$$

with the strength of the spin-spin couplings given by:

$$J_{i,j} = \sum_m \frac{b_{i,m}b_{j,m}\Omega_i\Omega_j\Omega_R}{2(\mu^2 - \omega_m^2)}. \tag{2.39}$$

In this equation, b is the normal mode coupling matrix to each ion and the interaction strengths are written proportional to the atom recoil frequency, $\Omega_R = \frac{(\Delta k)^2}{2M}$. These

long-range interactions fall off with a power law, $J_{i,j} \approx \frac{1}{|i-j|^\alpha}$, where α can be tuned between 0 and 3 as discussed below.

One can also generate an effective global σ_z field by asymmetrically detuning the red and blue sidebands about the normal modes of motion. In this case when choosing the appropriate rotating frame a global σ_z emerges from the first-order term in the Magnus expansion.

2.4   Influence of Normal Modes on the Interaction Profile

The ions' equilibrium positions are determined through the balance of the mutual electrostatic repulsion of the ions and the confining potential. In our trap the ions are tightly bound in the x and y direction and only weakly bound in the z direction and thus form a linear chain in this direction. Due to the ions' interaction their motion is coupled together and thus the motion of a single ion in a chain of N ions can be written in terms of N collective normal modes of motion. A detailed discussion of the calculation of the ion equilibrium positions and normal mode frequencies and eigenvectors is given in [57]. We use the higher frequency transverse normal modes of motion because they are less sensitive to thermal motion outside of the Lamb-Dicke limit and heating as a consequence of the stronger confinement [58].

One can think of the spin-spin coupling as arising from a modulation of the Coulomb interaction between the ions through the virtual excitation of the normal modes of motion. From this description and (2.39) it is clear that the spin-spin

coupling profile is determined by the normal mode structure. In this section I will discuss how we tune the range of the interaction and the inhomogenitiy of the nearest neighbor Ising coupling that arises from the normal mode profile and discuss its dependence on α.

To achieve longer range interactions (smaller α) one detunes closer to the center of mass mode, the highest frequency mode, or increases the axial confinement to increase the bandwidth of the transverse normal modes so that the coupling to the center of mass mode is stronger relative to the other modes. Because the center of mass mode is an all-to-all coupling this results in a long range interaction. However, in this case an inhomogenity in the nearest neighbor interactions, J_{NN}, arises as the highest frequency normal modes of motion (excluding center of mass) have a stronger coupling to the end ions than the center ions. Thus, J_{NN} is larger on the ends of the chain than in the center.

For shorter range interactions (larger α), one detunes further from the center of mass mode, or decreases the bandwidth of the normal modes so that the coupling to the center of mass mode becomes weaker compared to the lower frequency modes. Since these lower frequency modes do not couple to all of the ions equally this decreases the range of the interaction. Once again, there is an inhomogenity in J_{NN} due to the fact that the lower frequency normal modes of motion have a stronger coupling to the center ions, so J_{NN} in the center of the chain is larger than on the ends. This inhomogenity varies with increasing α from J_{NN} being larger on the ends to being larger in the center with roughly homogeneous couplings when $\alpha \approx 1.3$ as seen in Fig. 2.4. Although, there is a point where the coupling between the two

23
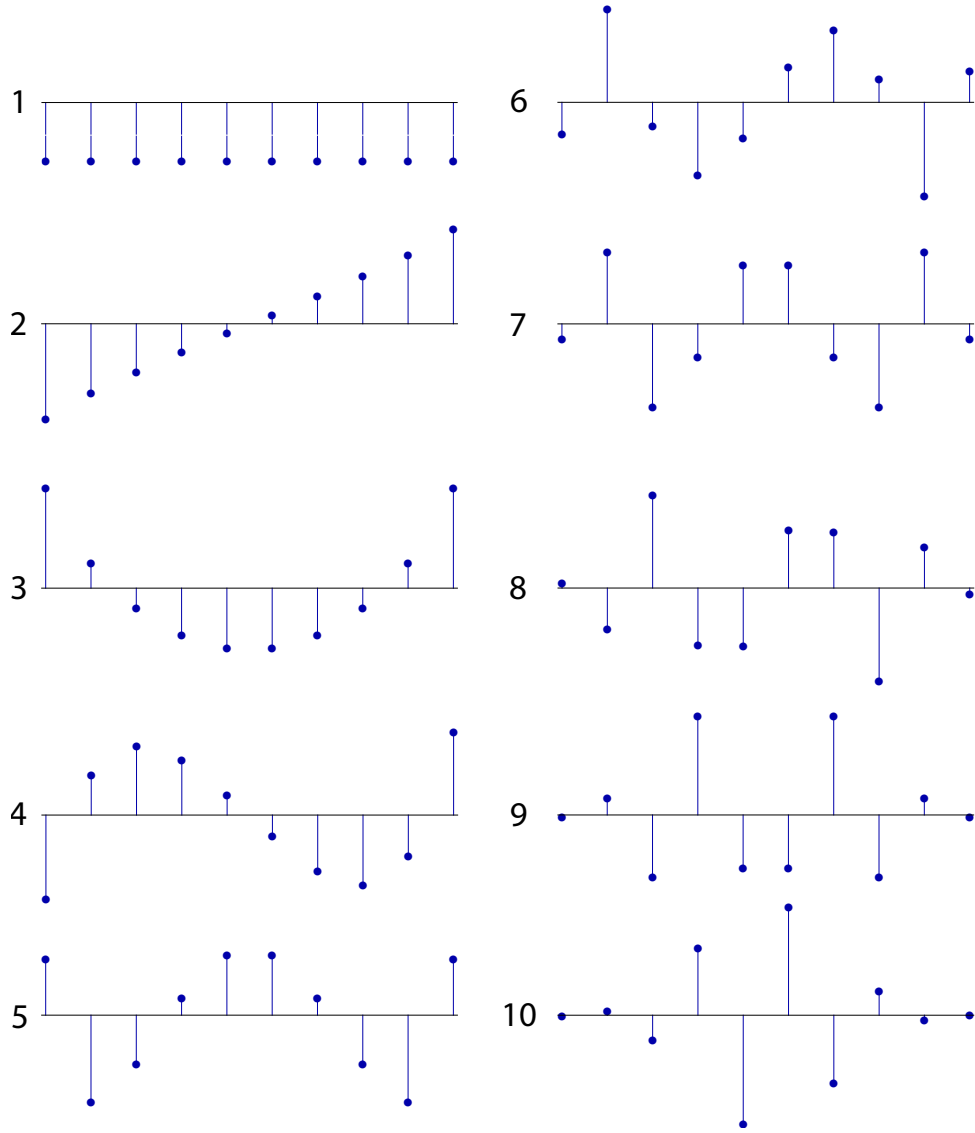
Figure 2.3: **Normal Modes.** Normal mode coupling coefficients for 10 ions from highest to lowest frequency. The first few high frequency modes have a stronger coupling to the end ions than the ions at the center of the chain resulting in J_{NN} being larger for the ends of the chain than for the center for longer range interactions. Conversely, the lower frequency modes have a stronger coupling to the center ions and thus J_{NN} is larger for the center than on the ends for shorter range interactions.

end ions and the center ions is equal, Fig. 2.5 makes clear that there is never a point where the nearest neighbor interactions are completely uniform since there is never a point where the standard deviation of J_{NN} is equal to zero. Moreover, from this plot it appears as if the value of α for which the couplings are most uniform is increasing with larger ion chains.

I will mention, but not discuss in detail, that there is a much less pronounced inhomogenity of the longer range interactions across the chain.
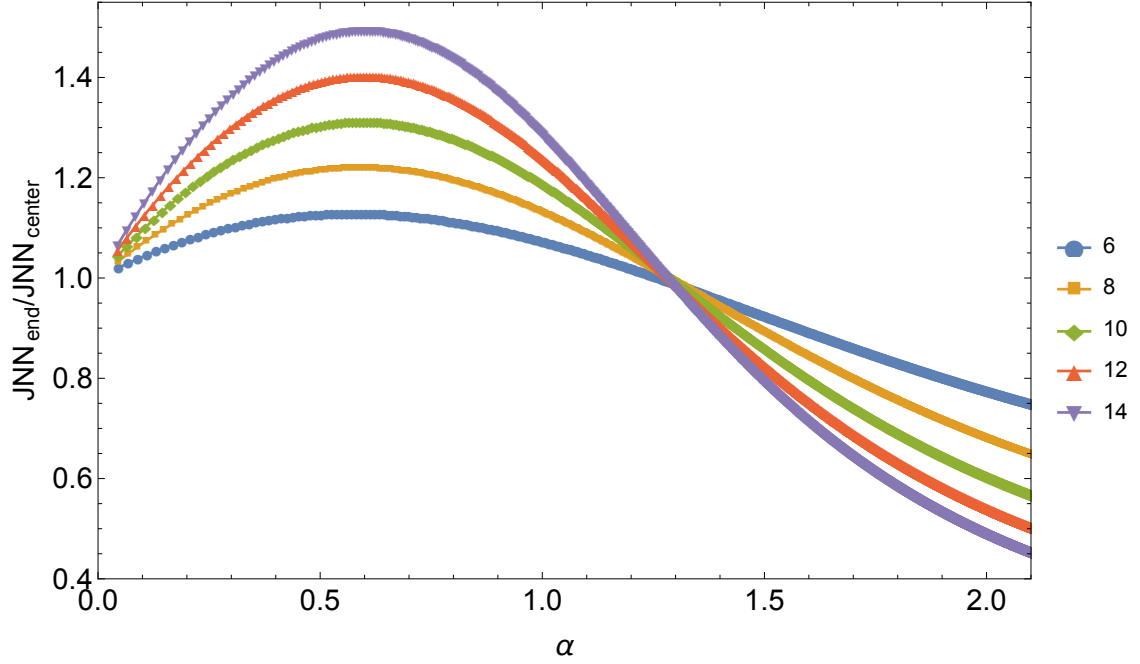
Figure 2.4: **NN Inhomogenity vs α.** Ratio of the nearest neighbor coupling strength between two end ions and the center ions for 6, 8, 10, 12, and 14 ions with respect to α. For longer range interactions (smaller α), J_{NN} is larger on the end of the chain due the stronger average coupling of the highest frequency normal modes to the end of the chain. However, as the interaction range becomes shorter (larger α) J_{NN} becomes large for center of the chain because the lower frequency normal modes couple more strongly to the center of the chain.
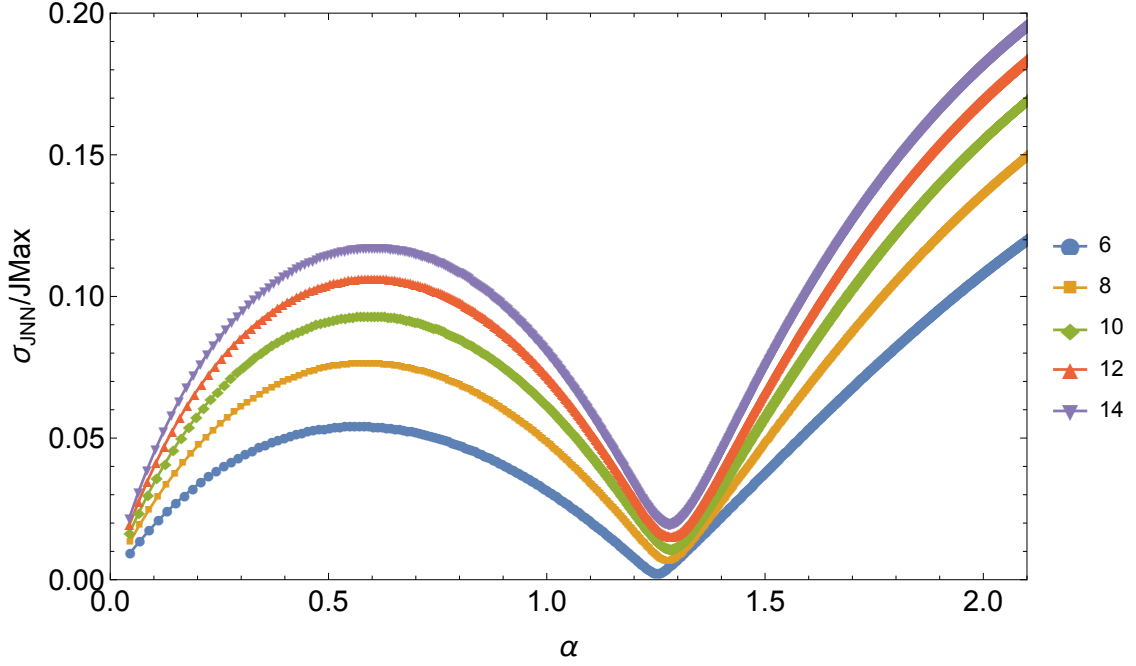
Figure 2.5: **NN Inhomogenity vs α Standard deviation.** Standard deviation of the nearest neighbor couplings for 6, 8, 10, 12, and 14 ions with respect to α. As also seen in Figure 2.4 the couplings are most homogenious at $\alpha \approx 1.3$. However, since the standard deviation is always non-zero there is never a point were the couplings are completely uniform. The value of α where the couplings are most uniform appears to be increasing with increasing ion number.

Chapter 3: Experimental Apparatus

In this chapter I will discuss our particular experimental setup for trapped ion quantum simulation. As mentioned earlier this is a mature project in a mature lab and thus, many of the details of the setup have been discussed in the theses of already graduated members of the quantum simulation lab [46–49] or other projects in the Monroe group. I will begin with a high-level overview and then jump into a more detailed discussion of the setup. I will expand on the astigmatism of the Raman beams, the individual addressing beam path, and our attempts to lock the frequency of the secular motion of the trap which are new since Crystal Senko's thesis [48].

3.1 Overview

We trap ions in a three-layer RF Paul Trap. An RF voltage is applied to the middle electrodes which confines the ions radially. The trap geometry results in a zero of the RF field along an axis of the trap referred to as the RF null. DC voltages are applied to the outer electrodes to provide axial confinement and to provide additional compensatory voltages to ensure that the ions are along the RF null. The trap is housed inside an ultra-high vacuum chamber which we believe to have a

pressure on the level of 10^{-11} Torr. Although this is a low pressure, the ion lifetimes are still limited by collisions between the ions and background gas molecules. This is a motivation for attempts to develop a cryogenic system at 4 K which which could potentially cryopump the pressure down a few orders of magnitude and lead to longer lifetimes [59].

Resonant light at 369 nm is used to cool, initialize (optical pumping), and detect the ions on the $\left|^2S_{1/2}\right\rangle$ to $\left|^2P_{1/2}\right\rangle$ transition. Ions in the low-lying $\left|^2D_{3/2}\right\rangle$ levels are repumped using 935 nm light. One unique feature of our lab is that we have additional far-detuned Doppler cooling beams at 48 MHz, 400 MHz, 800 MHz from resonance. The beam at 48 MHz is present to cool ions that are experiencing micromotion, which is motion at the RF drive frequency, and significantly increases cooling efficiency during loading when the trap RF is low. The cooling beams at 400 MHz and 800 MHz are present to cool the ions after a collision that are presumably hot. We photoionize in two steps: the first is provided by a 399 nm diode laser and the seconds either comes from a 369 nm laser or our 355 nm laser.

We collect the the detection florescence from the ions with an objective (NA = 0.23) which we image and then focus onto a PMT for calibrations and diagnostics or an ICCD camera for data taking. Using a camera enables site-specific readout of the ions which is essential for the data presented in this thesis. About 10% of the 369 nm light is focused onto a different PMT which we use to detect loss of the ions during the cooling cycle.

For coherent operations between the two effective spin states we use the beat-note between two pulsed laser beams that originate from a Coherent Paladin com-

pact 4 W laser. Because the repetition rate is chosen so that a single comb cannot drive the hyperfine transition, we use AOM's to make up the difference so that the beatnote can drive transitions. We use the zeroth order light from one of the AOM's used for coherent operations to apply site-resolved Stark shifts on the ions [45]. There is also a microwave horn present, that we use for diagnostics and the initial alignment of the Raman beams.

3.2   369 nm Resonant Laser Light and 399 nm Loading Light

We use 369 nm light to perform optical pumping (state initialization), Doppler cooling, and readout. Because we work with long ion chains and thus must expand our beams to globally address all of the ions we historically need ≈ 2.5 mw delivered to the trap which is more than the other experiments. Although, as I will discuss below, we may not need as much power when working with longer chains because our far detuned cooling beam does not effectively recool longer chains after a collision between an ion in the chain and a background gas molecule. The beam path for the resonant (369 nm), loading (399 nm), and repump (935 nm) light is schematically represented in Figure 3.1

Since we need so much laser power we use a Coherent MBR-110 Ti:Sapphire laser pumped by a Lighthouse Photonics Sprout-G-18W which provides 18 W of 532 nm, to produce 739 nm light. This laser is well documented in the Coherent manuals and in previous theses by [46] and [48]. Approximately 50 mW of this light is sent to a setup to perform Doppler-free spectroscopy on I_2 as documented in the

thesis of Andrew Chew [60]. At peak performance we have seen upwards of 1.75 W out of the MBR as measured after the pickoff for I_2 spectroscopy, but recently we have only managed about 1.2 W at this point. These numbers are well below what one could expect to for optimal performance of the MBR and are probably due to the fact that the cavity is not clean. This is supported by the fact that every time the power out of the MBR dips it can be recovered by cleaning the intra-cavity etalon.

The remaining 739 nm light that is not used for Doppler-free spectroscopy is fiber coupled into a polarization maintaining fiber (Coastal Connections 630 nm PM) using a Thorlabs PAF-X-11-B-FiberPort. Typically, this fiber coupling efficiency is greater than 60%. The output of this fiber is directed into in a Spectra Physics Wavetrain doubling system where it is frequency doubled to 369 nm. As a consequence of this fiber coupling the frequency doubler rarely needs to be realigned, however, a procedure for doing so is discussed in Senko's thesis [48].

As the light exits the doubler it is approximately 430 MHz detuned from the $\left|^2S_{1/2}, F = 1\right\rangle$ to $\left|^2P_{1/2}, F = 0\right\rangle$ transition and then is shifted to appropriate frequency using EOM's and AOM's. After the doubler there are three HWP's, two PBS's, and a thin film polarizer that allow the light to be arbitrarily redistributed to all of the different 369 nm beam paths.

The light that is reflected by the thin film polarizer after being transmitted by the first HWP and PBS pair is sent to an AOM (Brimrose QZF-420-40-370) where its frequency is shifted on resonance with the $\left|^2S_{1/2}, F = 1\right\rangle$ to $\left|^2P_{1/2}, F = 0\right\rangle$ transition. The RF source for this AOM is a PTS 500 frequency synthesizer from
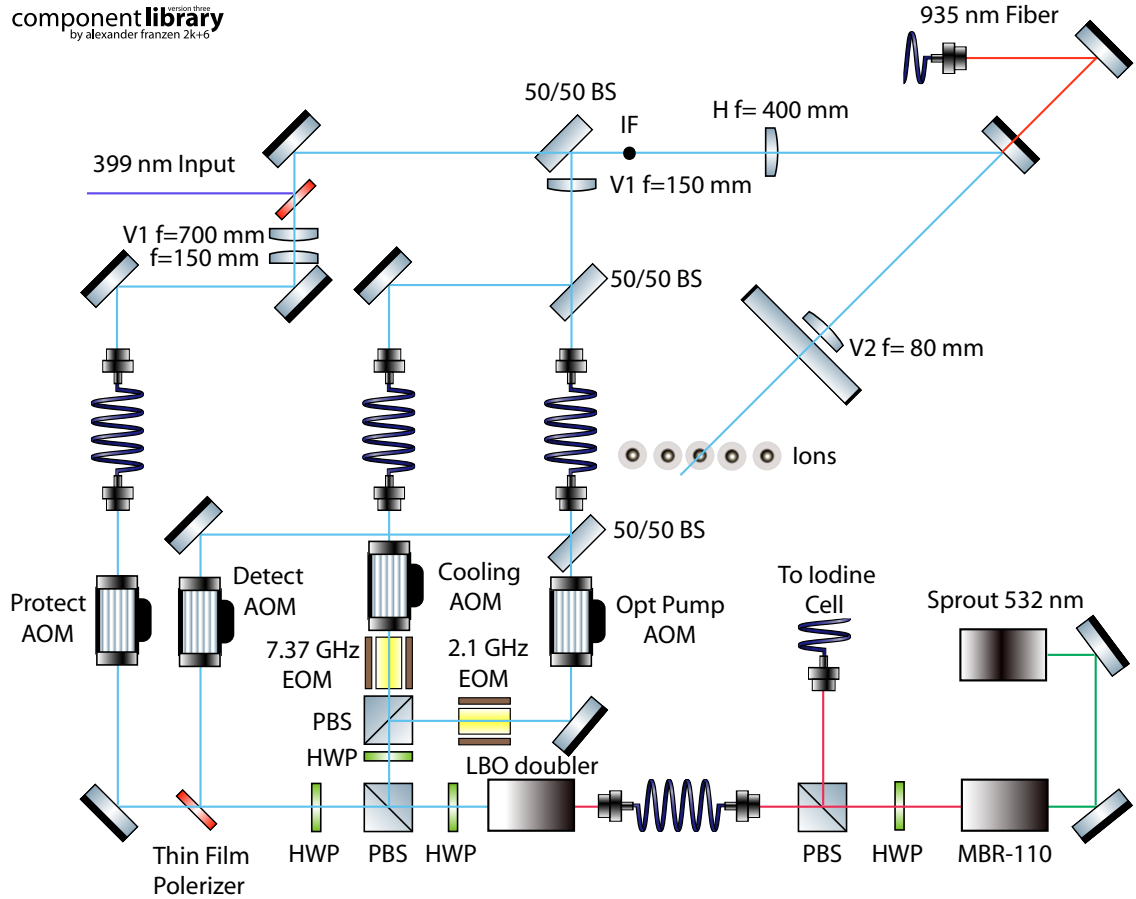
Figure 3.1: **Schematic Diagram of the 369 nm Beams.** A 532 nm laser pumps a Ti:Sapphire laser which outputs at 739 nm. We fiber couple this light to a polarization-maintaining fiber whose output we frequency double to 369 nm. This 369 nm light is split into several different beams for Doppler cooling, detection, and optical pumping. There are HWP PBS pairs that act as variable attenuators that allow for any arbitrary distribution of laser intensity into each of the beams. We couple all of the 369 nm light to fibers to spatially filter resonant laser light when the AOM is not being driven. After the fibers, all of the 369 nm beams are combined with the 399 nm loading beam and 935 nm repump and are focused down on the ions.

Programmed Test Sources inc. Because of dipole selection rules, $\Delta F = 0, \pm 1$ and $\Delta m_F = 0, \pm 1$, $\left|{}^2 P_{1/2}, F = 0\right\rangle$ only decays to the $\left|{}^2 S_{1/2}, F = 1\right\rangle$ (except for decay to a low lying $\left|{}^2 D_{3/2}, F = 1\right\rangle$ state) creating a closed cycling transition which allows for efficient state-dependent detection between the $\left|\downarrow\right\rangle$ and $\left|\uparrow\right\rangle$ states.

This florescence is collected by a imaging objective CVI (UVO-20.0-10.0-355-532, NA=0.23) and is then magnified by a factor of ≈ 130 by a doublet lens pair and is slowly focusing onto either a camera (Princeton Instruments PIMax: 1024i ICCD, for a detailed description see [61]) or a PMT (Hamamatsu H10682-210) based on the position of the flipper mirror as seen in Figure 3.2. The PMT has an additional lens to demagnify the image so that it fits on the detector. The camera and imaging objective are being updated with a new custom objective with NA=0.4 which will allow for more light collection and an Andor iXon Ultra 897-EX EMCCD camera.

There is an adjustable aperture (Thorlabs SM1D12CZ) at the image plane of the objective that filters out light scatter that is not from the ion. We replaced the previous fixed pinhole with the adjustable one because it was clipping the individual addressing beam and was thus limiting the number of ions that could be individually addressed. The amount of background scatter does not decrease when we close the aperture which seems to indicate that it is not at the image plane of the objective, so when the new 369 nm imaging system is installed it will allow for the tuning of the distance between the aperture and the objective lens.

In the camera and PMT beam path there are Semrock LP02-355RS-25 and FF01-370/10-25 to filter out 355 nm and other background light. An additional Semrock FF01-370/10-25 is in the PMT beam path in order to further filter out the
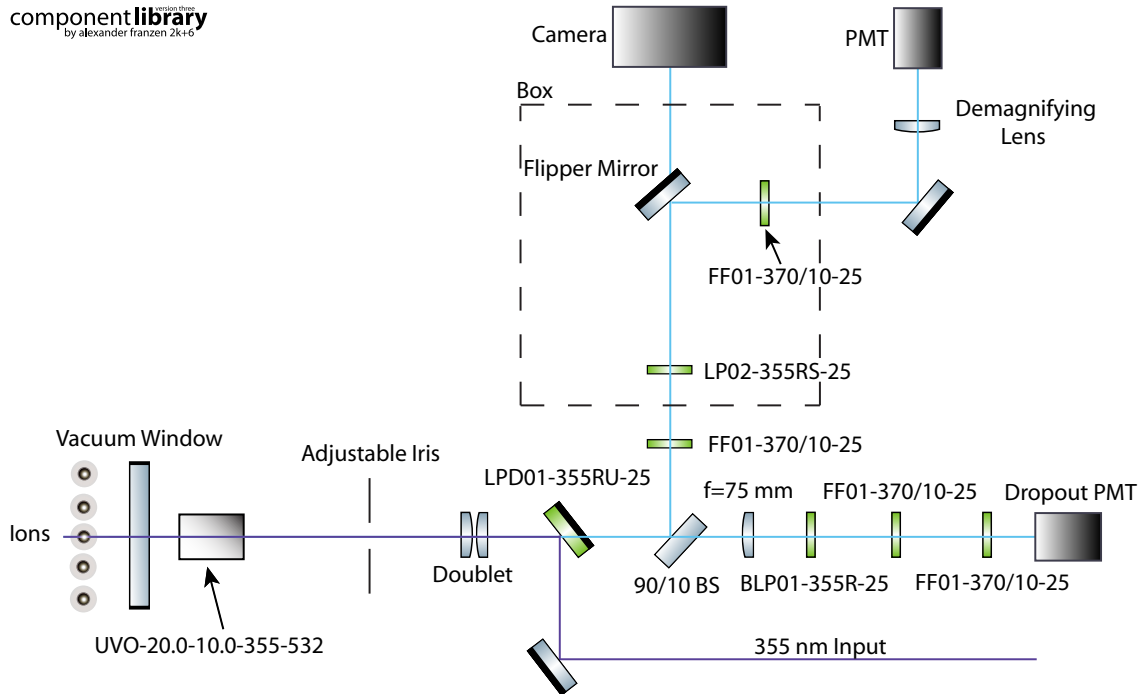
Figure 3.2: **Schematic Diagram of Ion Imaging Optics.** The 369 nm florescence from the ion is collected with an off-the-shelf imaging objective with NA of 0.23 which is also used to tightly focus the individual addressing beam. The light at 369 nm is magnified by a factor of ≈ 130 and slowly focused onto either a camera or PMT depending on the position of the flipper mirror. 10% of the 369 nm florescence is sent to a dropout detection PMT. The individual addressing beam is combined with the 369 nm beam path using a dichroic beam splitter. There are several filters in the beam paths to the camera and PMT's in order to filter out room light and scatter from the individual addressing beam.

355 nm light that enters into the imaging system due to the individual addressing beam. This filter is not needed in the camera path because the camera intensifier is off during the application of the individual addressing beam.

10% of the 369 nm light is picked off and sent to an additional PMT which is used to monitor fluorescence counts during cooling to determine if the ions are in the trap. If the cooling fluorescence counts drop below a certain threshold for a given number of consecutive cooling cycles the control program interrupts the experimental sequence and lowers the trapping RF and applies full cooling power and the additional far detuned cooling frequencies. Because our ability to recapture ions after a background gas collision depends on how quickly additional cooling power and the farther detuned cooling beams can be applied to the ions, the probability of a successful recapture increases greatly as compared to having the experiment operator determine if ions were lost and applying the ion recapture scheme.

In order to efficiently determine if the ions are still in a linear chain during cooling it is important that the number of background counts on the PMT due to other sources of light is small. This is achieved by including two Semrock FF01-370/10-25 filters and a Semrock BLP01-355R-25 filter. However, when we installed the second FF01-370/10-25 filter there was still a significant amount of background scatter that seemed to be from the individual addressing beam so installing an additional 355 nm filter such as another Semrock FF01-370/10-25 or a LPD01-355RU-25 may further lower the background counts.

The 369 nm light that is reflected by the first HWP and PBS pair and transmitted by the second pair is used for Doppler cooling on the transition $\left|^2S_{1/2}\right\rangle$

to $|^2P_{1/2}\rangle$. In order to cool both the $|^2S_{1/2}, F = 0\rangle$ and the $|^2S_{1/2}, F = 1\rangle$ states, this light is first sent through a resonant New Focus EOM at 7.37 GHz. Cooling of both states is necessary because at the end of an experiment some ions are in the $|^2S_{1/2}, F = 0\rangle$ and there is some probability of off-resonantly exciting the $|^2S_{1/2}, F = 1\rangle$ to $|^2P_{1/2}, F = 1\rangle$ transition which can decay to the $|^2S_{1/2}, F = 0\rangle$ state. The second order sideband is at 14.74 GHz, which is equal to the combined hyperfine splitting of the $|^2S_{1/2}\rangle$ and $|^2P_{1/2}\rangle$ states. The RF drive for this EOM is $\approx$0.5 W after amplification and is supplied by a Vaunix Lab Brick signal generator.

The light is then sent through an AOM (Brimrose QZF-420-40-370) that frequency shifts the first order beam to a half a linewidth away from the $|^2S_{1/2}, F = 1\rangle$ to $|^2P_{1/2}, F = 0\rangle$ and the $|^2S_{1/2}, F = 0\rangle$ to $|^2P_{1/2}, F = 1\rangle$ transitions for the EOM carrier and second order sideband beams, respectively. This is the detuning that gives the most efficient Doppler cooling. This AOM is driven by an amplified signal from a HP8640B which is sent through a computer controlled VCA to allow for continuous control of the RF power.

The zeroth order of this AOM is used as a far detuned cooling beam, which we refer to as "protection plus" for when the chain suffers a background gas collision. Because of the beam's high power, it can cool a large range of ion velocities. This beam must be blocked using a physical shutter because it is the zeroth order output of an AOM, the other beams are modulated using the RF drive to the AOM. Because of the speed of mechanical shutters, this beam must be blocked during the experimental cycle and thus further underscores the importance of the aforementioned drop-out detection.

The light that is reflected by both pairs of HWP's and PBS's is used for global preparation of the $\left|{}^2S_{1/2}, F = 0\right\rangle$ state through optical pumping. This light is first sent through a resonant New Focus EOM at 2.105 GHz which is equal to the hyperfine splitting between the $\left|{}^2P_{1/2}\right\rangle$ levels. This EOM is driven by a HP8671A and its strength is tuned such that power in the carrier mode is zeroed. The light then pass through an AOM (Brimrose QZF-420-40-370) whose first diffracted order is on resonance with $\left|{}^2S_{1/2}, F = 1\right\rangle$ to $\left|{}^2P_{1/2}, F = 1\right\rangle$. Since the $\left|{}^2P_{1/2}, F = 1\right\rangle$ levels have some probability of decaying to the $\left|{}^2S_{1/2}, F = 0\right\rangle$ driving this transition can prepare $\left|{}^2S_{1/2}, F = 0\right\rangle$ with high fidelity.

The last 369 nm beam is another far-detuned cooling beam which we refer to as the "protection" beam which is the transmitted light from the first PBS and the thin film polarizer. This light passes through an AOM (IntraAction ASM-4001LA8.18) and its negative first order diffracted beam is $\approx$ 800 MHz off-resonance of the $\left|{}^2S_{1/2}, F = 1\right\rangle$ to $\left|{}^2P_{1/2}, F = 0\right\rangle$ transition. The large amount of power in this beam, just as with the "protection plus" beam, and the large detuning results in cooling ions over a large range of velocities, however, it is unable to cool the $\left|{}^2S_{1/2}, F = 0\right\rangle$ state.

All of the 369 nm light is coupled to optical fibers to spatially filter resonant light scatter from the AOM's. 400 MHz AOMs are used in order to achieve large deflection angles between the zeroth and first diffracted order beams out of the AOM and to ensure the zeroth order light is far off-resonance. There is a really nice summary figure of all of the 369 nm light in [48].

The optical pumping and detection beams are combined on a 50/50 BS before

being coupled to fiber and the rest of the 369 nm beams are combined on 50/50 BS's after the optical fibers. The light is vertically focused at an intermediate focus by V1 which is then imaged onto the ions by V2 with a magnification factor 1/5. An improvement to the current optics setup would be to move the 369 nm fiber output closer to the chamber which should improve beam pointing stability.

Loading is achieved using a two step ionization process which is described in detail in [62]. The first step is provided by a photon from a 399 nm laser. The second is traditionally provided by a 369 nm resonant photon, but we have found that it is much more efficient to use the 355 nm beam as the second step of ionization because of the high power in that beam. The 399 nm laser comes from a Toptica (DL100) grating-tuned external cavity diode laser and is combined with the protection beam after the 369 nm fiber with a Semrock dichroic beamspliter FF380-Di01-25x36.

As previously noted there is some probability for population to decay into the $\left|^2D_{3/2}\right\rangle$ levels. We repump this population into the $\left|^2S_{1/2}\right\rangle$ state by applying 935 nm laser light on resonance with the $\left|^2D_{3/2}\right\rangle$ to $\left|^3[3/2]_{1/2}\right\rangle$ transition because the $\left|^3[3/2]_{1/2}\right\rangle$ contains some of the $\left|^2P_{1/2}\right\rangle$ state and $\left|^2P_{1/2}\right\rangle \leftrightarrow \left|^2D_{3/2}\right\rangle$ and $\left|^2P_{1/2}\right\rangle \leftrightarrow \left|^2S_{1/2}\right\rangle$ are dipole-allowed transitions [48]. A Toptica (DL100) grating-tuned external cavity diode laser provides this light. The frequency is stabilized by feeding back to a piezo to control the grating angle using software to lock a frequency measurement on a wavemeter (High Finesse WSU). The laser frequency is on resonance with the $\left|^2D_{3/2}, F = 1\right\rangle$ to $\left|^3[3/2]_{1/2}, F = 0\right\rangle$ transition. The light passes through a fiber EOM from EOSpace driven at 3.0695 GHz and adds sidebands at the drive frequency which are at approximately 2% of the carrier. The

lower sideband is used to drive the $\left|{}^2D_{3/2}, F = 2\right\rangle$ to $\left|{}^3[3/2]_{1/2}, F = 1\right\rangle$ transition. This light is combined with the 369 nm and loading light using a dichroic mirror.

Under current experimental conditions (I optimized the fiber coupling of each beam before the measurement) the power in all of the laser beams as measured by the FieldMate Laser Power Meter set on $\lambda = 399$ nm and directly after their respective fiber couplings unless otherwise noted are:

Power out of the doubler - 27 mW

Loading power (measured before M1) - 1.8 mW

Cooling power (measured at a cooling VCA setting of 5) - 443 μW

Protection power - 400 μW

Protection plus power - 600 μW

Optical pumping power - 204 μW

Detection power - 8.5 μW

3.3   355 nm Raman Laser Light

I will now discuss the 355 nm optics setup that is used to deliver the 355 nm light from a Coherent Paladin compact 4 W laser from the output of the laser to the ions. The Raman setup is also documented in [48]. In this thesis I will give an an overview of the Raman optics setup and discuss the astigmatism of the light at the ions that is a consequence of using lenses whose focal lengths are defined for different wavelengths.

After the 355 nm light exists the Paladin laser it encounters a pickoff window

whose reflection is sent to a fast photodiode (Alphalas UPD-30-VSG-P) used for the beatnote stabilization lock [48, 63] as seen in Figure 3.3. The transmitted light through the pickoff window then reaches a HWP and PBS used as a variable attenuator for the light reaching the ions. The light is then split into two paths by a 50/50 BS for the two Raman beams.

The two Raman beam paths are identical except we use the zeroth order light from the Raman 2 AOM for the individual addressing beam, the AOM in the Raman 2 beam path has multiple frequencies applied to it, and there is a delay stage in the Raman 2 beam path to match the optical path length of the two Raman arms. Thus, I will only discuss the Raman 2 path in detail, but both paths can be seen in Figs. 3.3, 3.4.

After the 50/50 BS there is a HWP used to tune the polarization to give the maximum diffraction efficiency from the AOM (typically $\approx 50\%$). The light then passes through a f=100 mm lens which focuses the light through the AOM (Brimrose QZF-210-40-355) so that the AOM can be imaged. We want to image the AOM because we apply multiple frequencies simultaneously to generate the spin-spin couplings and we want the output of the ions at these different drive frequencies to overlap at the ions. As mentioned, the zeroth order light is picked off for the individual addressing beam path using a D-mirror and is re-collimated using a f=400 mm lens. The first order output of the Raman 2 AOM is re-collimated with a f=250 mm lens.

The light is then sent through a telescope consisting of a f=250 mm plano-convex lens, a f=100 mm horizontal cylindrical lens and a f=500 mm vertical cylin-
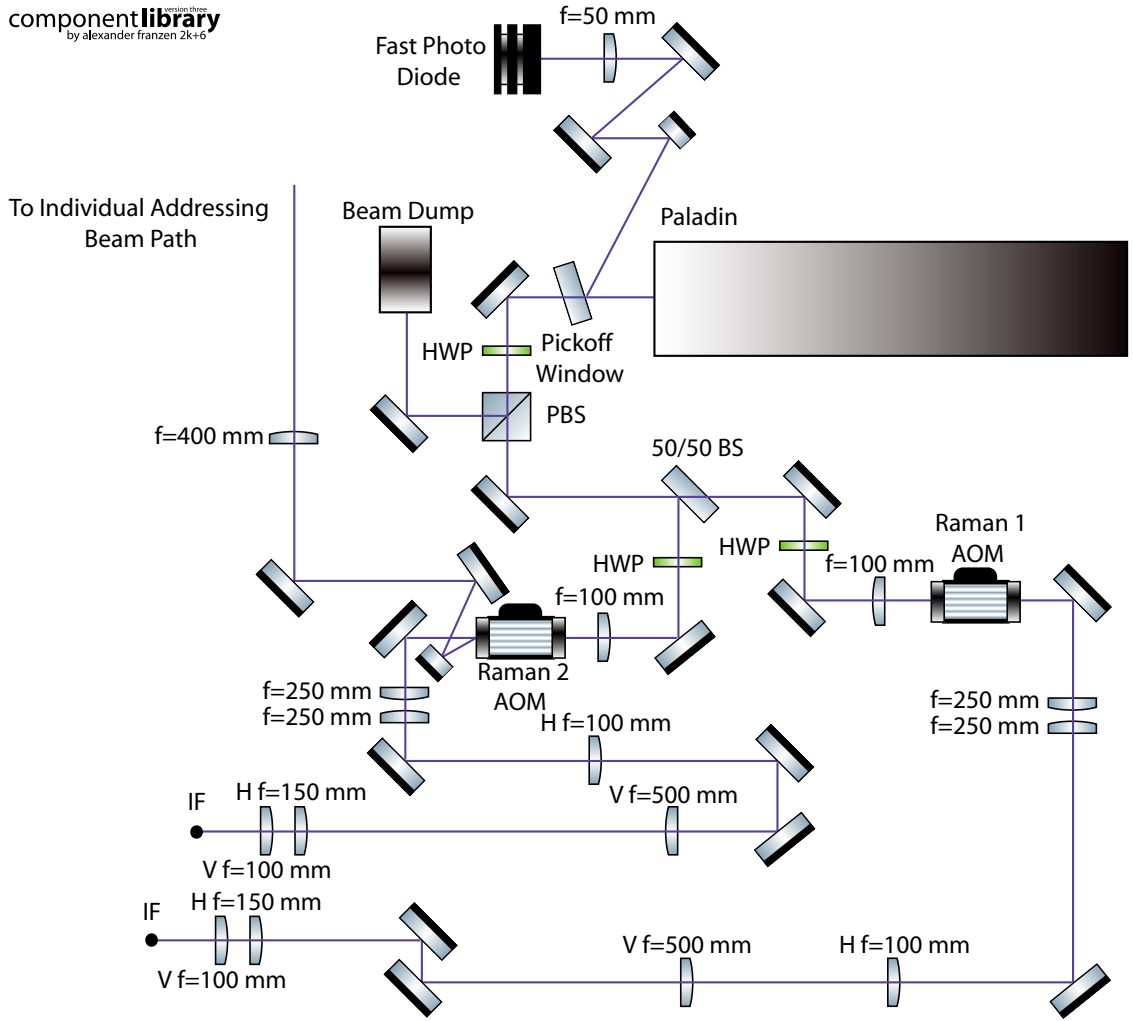
Figure 3.3: **First Half of 355 nm Beam Path.** The 355 nm pulsed laser light is provided by a Coherent Paladin 4 W laser. Some of this light is picked off from the main beam path for the beat-note stabilization lock. The rest of the light is broken up into two beams that each pass through imaged AOM's, are beam shaped with telescopes, and are focused at an intermediate focus which is later imaged onto the ions. The zeroth order light from the Raman 2 AOM is used for individual ion addressing.
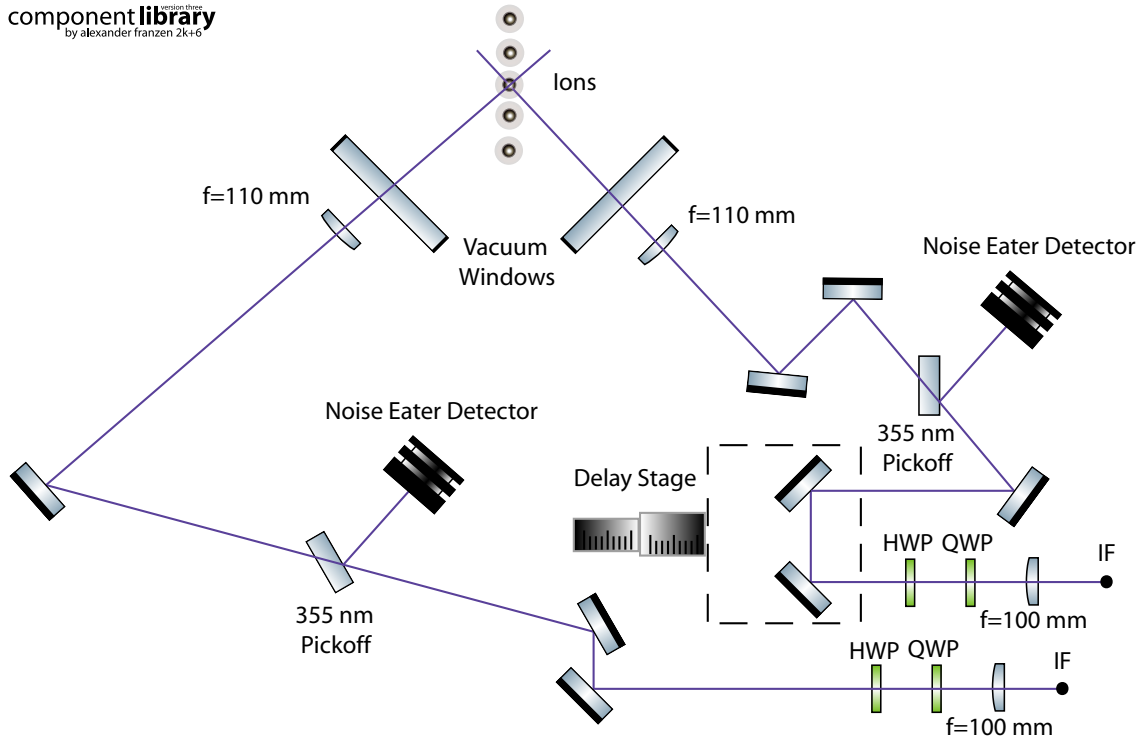
Figure 3.4: **Second Half of 355 nm Beam Path.** After the intermediate focus, the beam is recollimated with a f=100 mm lens and encounters a QWP and a HWP to ensure maximum coupling between the two effective spin states. Afterward, there is a pickoff window to divert light to a photodiode that will be used to monitor laser intensities for noise eating. There is a delay stage in the Raman 2 beam path so that the length of the Raman 1 and 2 beam paths can be matched. Since the beams hit the ions at a 45 degree angle the effective horizontal beam waist is a factor of $\sqrt{2}$ larger.
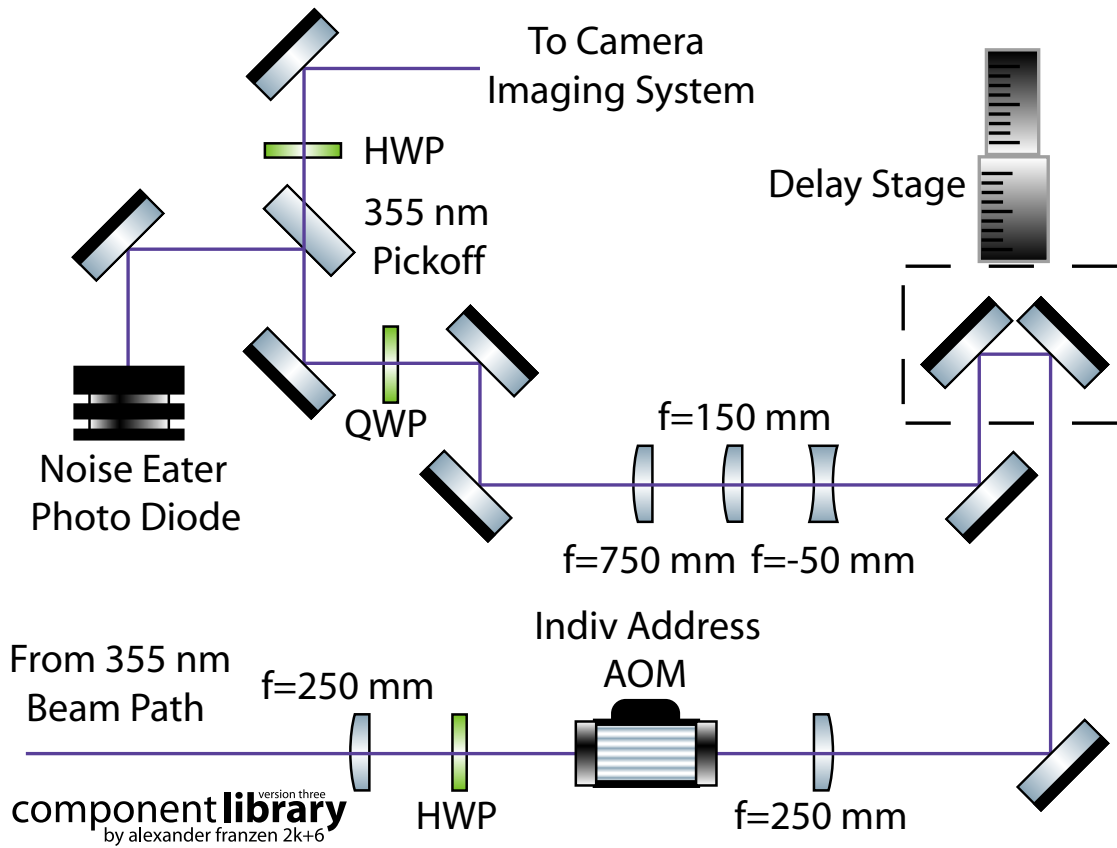
Figure 3.5: **Individual Addressing Beam Path.** After the Raman 2 AOM the individual ion addressing light passes through an AOM that is not imaged so that different diffraction angles correspond to a different laser beam position at the ions. After the AOM the light passes through a telescope consisting of a negative lens with f=-50 mm and a lens with f=150 mm. The light then pass through a slow lens which matches the 355 nm beam to the 369 nm camera imaging system. There are also waveplates in this beam path to set the beam polarization correctly. Some of the light is picked off for a sample and hold noise eater.

drical lens. Afterward, the light is focused down with a horizontal cylindrical lens of f=150 mm and a vertical cylindrical lens of f=100 mm to a beam waist, in principle, of 10 μm vertically and 100 μm horizontally at the intermediate focus. In reality, when imaging the spot size at the intermediate focus we see that it is really 9 μm vertically and 90 μm horizontally.

This is the optimal vertical beam waist in terms of sensitivity to pointing instability. We determined this by measuring the decay time of oscillations due to a Stark shift from the red and blue sidebands during a Ramsey experiment. We saw that the decay time is shorter when the Raman beams were more tightly focused in the the vertical direction and unchanged when the Raman beams were less tightly focused in the vertical direction.

After the intermediate focus the beams are then recollimated using a f=100 mm spherical lens. The beam is then focused down onto the ions using an f=110 mm best form lens which is a lens that consists of two spherical surfaces but has be optimized for reduced spherical aberration. This imaging system consisting of the f=100 mm spherical lens and f=110 mm best form lens has a magnification of $\approx$ 1:1 between the intermediate focus and the ions.

There is also a delay stage in the Raman 2 beam path in order to match the path lengths of the two beams so that the pulses in each arm hit the ions simultaneously. The light also passes through a QWP and HWP to set the polarization of the beam so that the light only couples between the $|\downarrow\rangle$ and $|\uparrow\rangle$ states and there is no coupling to the Zeeman levels. There is no coupling to the Zeeman levels when the beams are horizontally polarized (not accounting for the birefringence of the

vacuum window).

An imperfection in the Raman beam setup is astigmatism between the focal positions in the vertical and horizontal directions due to using lenses with focal lengths defined for different wavelengths. We determine the degree of astigmatism by placing a mirror right before the vacuum chamber in the Raman 1 beam path and reflecting the light onto a camera that is at the same effective optical position as the ions. We then fit the following equation for the beam waist to the data:

$$\omega(z) = \omega_0 \sqrt{1 + \left(\frac{z - z_0}{z_R}\right)^2}. \tag{3.1}$$

Where ω is the beam waist, z_0 is the position of the focus, z is the axial position, and z_R is the Rayleigh range. This fit along with the directly measured beam waists can be seen in Fig. 3.6. There is clearly astigmatism present as the location of the focus in the horizontal and vertical direction are different (Final lens position of 0.291 in. for the vertical focus vs. 0.717 in. for the horizontal focus). With normal operating conditions we measure the beam waist at the ions to be 9 μm vertically and 93 μm horizontally.

Although, a horizontal waist of 93 μm is rather large we find that it is not large enough to provide uniform laser intensity for longer chains. For a chain of 26 ions with an axial harmonic potential with frequency of 500 Hz for a horizontal beam waist of (accounting for the factor $\sqrt{2}$ because of the angle of the Raman beams with respect to the ions) there would be a ~5 % variation in the Rabi frequency across the

chain. This is problematic for global state preparation and measurement of the ions along any direction of the Bloch sphere because these operations require uniform Rabi frequencies along the length of the chain. In the current system we addressed this issue by defocusing the Raman beams to achieve a large horizontal beam waist, but this results in a substantial amount of laser power being thrown away and much lower laser intensity at the ions. Thus, in future setups using long ion chains it would be most efficient to use a diffractive optic or some other beam shaping optical element that could deliver a top-hat beam profile at the ions. Because, working with a horizontal beam waist of 93 μm results in only $\sim$ 15 % of the total laser power in the full Gaussian beam being delivered to the ions for a chain of 10 ions with an axial harmonic potential of 500 Hz ($\sim 25\mu$m chain length).

There is a 355 nm pickoff window in both Raman beam paths that will eventually be used to monitor their intensities in order to correct for laser intensity fluctuations. The photodiode signal will be fed to a PID lock which will feed back to the AOM's in each respective arm. There is an additional complexity in the case of noise eating on the Raman 2 beam in that the RF drive is often lowered during the experimental evolution to perform adiabatic ramps. Thus, the set point of the PID lock will also need to be ramped so the lock point will follow the RF drive.

As mentioned above, the zeroth order light from the Raman 2 AOM is used for an individual addressing beam that allows for the application of site-resolved arbitrary Stark shifts on the ions whose beam path is detailed in Figure 3.5. After the zeroth order light is recollimated by the f=400 mm lens in Figure 3.3 it is focused down with an f=250 mm lens and passes through a HWP so that the polarization can
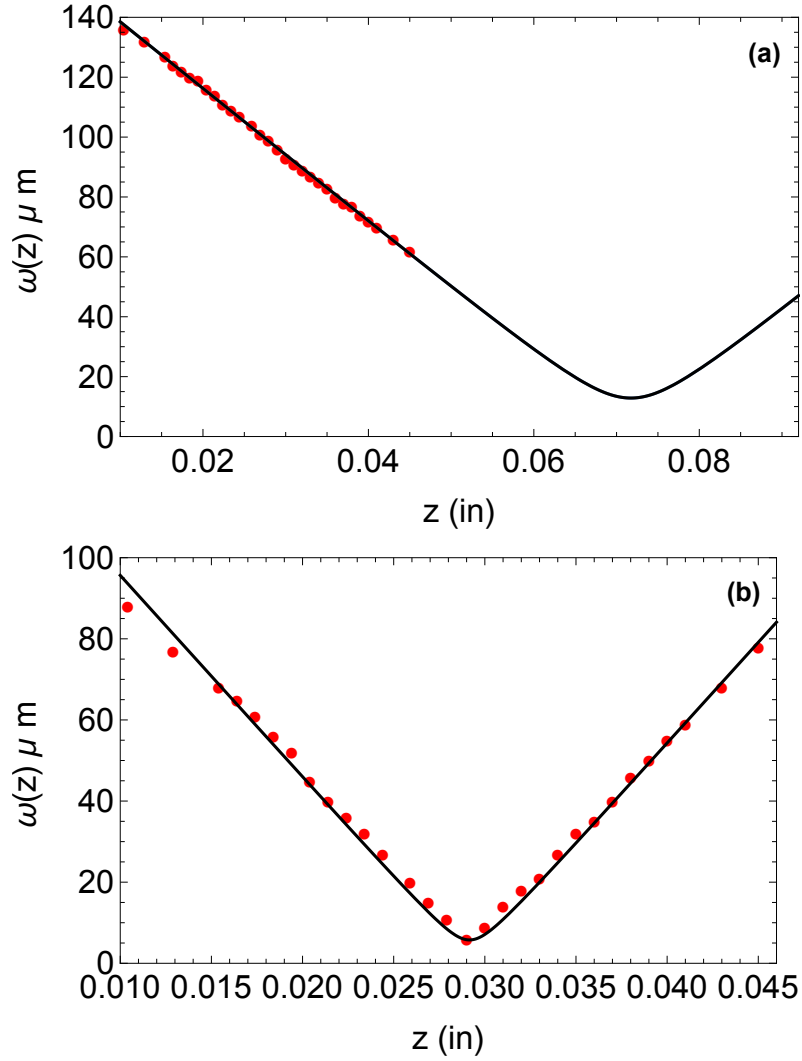
Figure 3.6: **Raman Beam Astigmatism.** Horizontal (a) and vertical (b) beam waists respectively of Raman one at the ion position with respect to the position of the final lens before the chamber. Clearly the beam is astigmatic as the focul points in the vertical direction (final lens position of 2.91) and the horizontal direction (final lens position of 7.17) are different

be tuned for optimal diffraction efficiency (as with the Raman beams the diffraction efficiency is typically 50%). The AOM is not placed at the focus of the beam so that the output of the AOM is not imaged. This is done so applying different RF frequencies results in a displacement of the individual addressing beam at the ions.

The beam is then recollimated with a f=250 mm lens. It encounters a delay stage which was installed so that the length of the individual addressing beam path can be matched with the length of the Raman beam path so the pulses from the individual addressing beam can hit the ion at the same time as the pulses from the Raman beams if there were ever a reason to do so. The light then impinges on a telescope with a magnification of 3 consisting of a negative lens of f=-50 mm and a plano convex lens of f=150 mm. After the telescope, the beam passes through a slow lens with a focal length of f=750 mm which was chosen using Zmax to ensure that there would be tight focus at the ions after the light passes through the 369 nm imaging system (a horizontal beam waist of less than 3 μm [45]).

There is a HWP and QWP after the slow lens to set the polarization to the value which gives the largest fourth-order Stark shift which, as mentioned in the previous chapter, is when the light is polarized $1/2\hat{\sigma}_- + 1/\sqrt{2}\hat{\pi} + 1/2\hat{\sigma}_+$ along the ion axis of quantization. This is achieved when the light's polarization is an equal superposition of vertical and horizontal polarization along the beam propagation direction. After the polarizers, the beam is then combined with the 369 nm imaging system.

There is also a piece of glass which picks off some of the 355 nm light and monitors it on a photo diode. This lock is a sample and hold lock with proportional

and double-integral gain, which samples the intensity of the individual addressing beam during the Doppler cooling cycle, compares it to a set point, and holds at the output value of the proportional and double-integral filter (New Focus LB1005 High-Speed Servo Controller) during the interaction cycle of the experiment.

3.4   Trap RF Stabilization

We confine ions by applying RF and DC voltages to electrodes in a three-layer RF Paul trap [46–48]. The RF voltage is supplied by an HP 8640B at about 38 MHz and passes through an amplifier. We further increase this voltage with a quarter-wave helical resonator (the can) which increases the voltage by the quality factor, Q, of the resonator.

From the discussion in the previous chapter it is clear the effective spin-spin couplings in our system depend on the secular trapping frequency. Thus, it follows that if the the secular trapping frequency is unstable, the spin-spin couplings will be as well. The secular frequency of the ions' motion [62] if given by:

$$\omega_{trap} = \frac{eV_0}{2^{1/2}m\Omega_T R^2},\tag{3.2}$$

where e is the charge of the electron, V_0 is the voltage of the RF drive, m is the mass of a $^{171}\text{Yb}^+$ ion, Ω_T is the RF drive frequency delivered to the trap, and R is the distance from the RF electrodes to the ions. Since the charge, trap geometry, and mass are fixed the only sources of noise on the secular frequency can come from

noise on V_0 or on Ω_T. Ideally, one would like to stabilize $\frac{V_0}{\Omega_T}$, but we instead lock the RF voltage delivered to can and Ω_T to the resonance of the can as detailed below.

When a background gas collides with an ion, the chain destablizes and we lower the trap RF to facilitate cooling of the ions. This is done by switching to a RF path with a VCA which is used to lower the RF delivered to the trap. We do this because we believe the RF heats the ions when they are not on the RF null. This process of lowering and raising the RF results in $\sim$1-5kHz drift in ω_{trap} which relaxes back to the value before recrystalizaion after approximately the time the RF was lowered. Traditionally, we compensate for this by simply waiting to continue taking data for the length of time the RF was low before continuing with experiments.

We lock Ω_T to the resonance of the can by minimizing the reflection from the can which is done by locking the phase of the reflected signal as seen in Figure 3.7. The phase of the reflected is mixed with a fixed phase delay. This value is then locked using a home built PID which feeds back onto the frequency of the HP8640B Signal Generator.

This value is locked because if Ω_T is not on the can resonance, then there will be less power delivered to the trap. During the course of a recrystalization cycle we find that the can resonance drifts by $\sim$1-2 kHz. Looking at equation 3.2, this seems like it would only account for a secular frequency change of a few Hz out of $\sim$4.8 MHz. Thus, this drift in Ω_T does not account for the drift we see in the secular frequency [48].

As a result, we have investigated if the drift in the secular frequency after recrystalization is due to changes in the RF power delivered to the trap. When
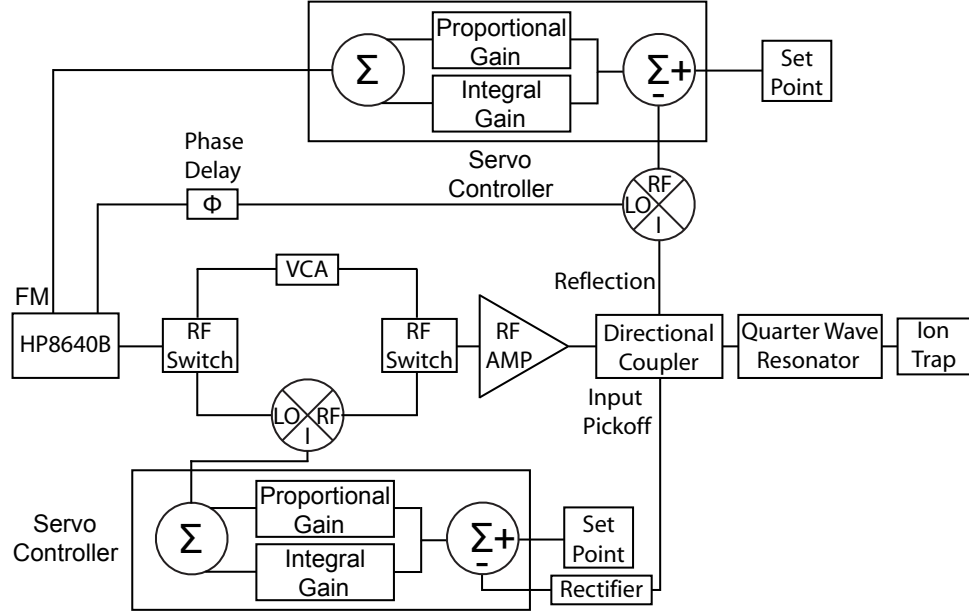
Figure 3.7: **Trap RF Stabilization Diagram.** The RF voltage for the trap is supplied by a HP8640B signal generator. The main output goes through an RF switch, which directs the RF through either a VCA used to lower the RF power, or a mixer used to lock the RF power. Afterward, the two paths are recombined and then pass through an RF amplifier and then a bi-directional coupler whose forward output is connected to the can, which steps up the voltage to the trap. The forward pickoff of the bi-directional is sent to a rectifier whose signal is sent to a PID to lock the RF power delivered to the can. The reflection pickoff is compared with a fixed phase delay and sent to a PID to ensure Ω_T follows the can resonance.

directly measuring the RF power supplied to the can we saw a shift that was roughly the same size and relaxed on the same timescale as the trap secular frequency. This motivated looking into drifts in the RF power applied to the can as the explanation for the drift in the secular frequency.

Further evidence pointing to noise on the RF power accounting for changes in the trap secular frequency can be seen in a plot of the time evolution of the average photon counts with two ions when stopping at the $5\pi/2$ time during Mølmer-Sørenson flopping and the time evolution of the RF supplied to the can as measured by monitoring the forward pickoff of a bi-directional coupler (Mini-Ciruits ZFBDC20-62HP-S) with an RF rectifier [50] as displayed in Figure 3.8. It is clear that the fluctuations in both of these quantities change together.

This point is further established if one looks at the Allan deviation [64,65] for this measurement. The Allan deviation is given by:

$$\sigma_y(\tau) = \sqrt{\frac{1}{2}\langle(\bar{y}_{n+1} - \bar{y}_n)^2\rangle}, \tag{3.3}$$

where τ is the sample period, $\bar{y}_n$ is the average value of the measurements made during τ, and the expectation value is taken over the total sample time.

The Allan deviation was developed because for common types of noise present in atomic clock experiments such as $1/f$ or white noise the traditional standard deviation is divergent. The Allan deviation, $\sigma_y(\tau)$, represents the deviation of the measurement over a period τ. It is clear from Figure 3.9 that the Allan deviation
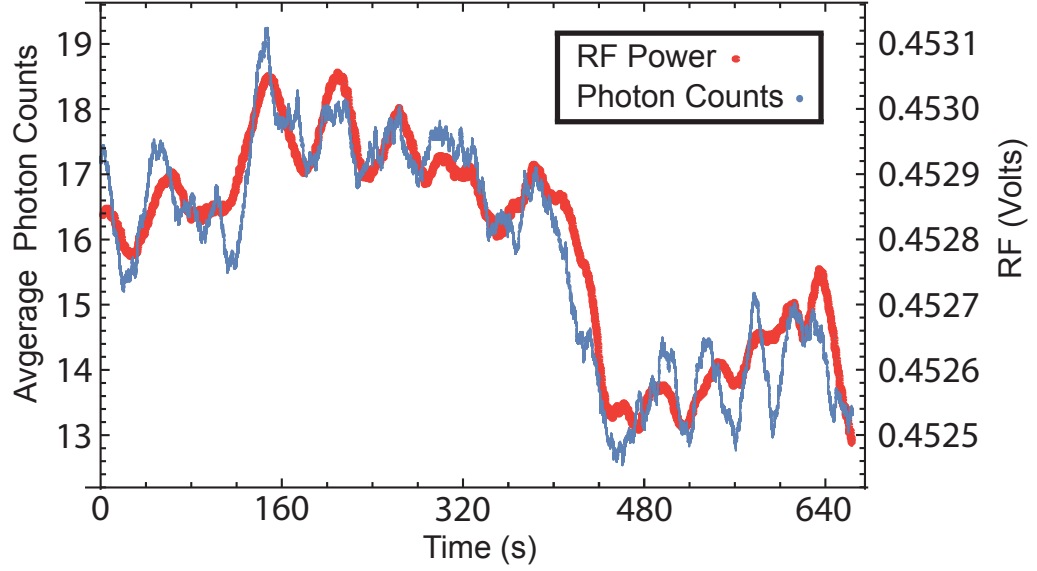
52

Figure 3.8: **Average Photon Counts and RF Voltage vs Time Without the RF Lock.** The flucuations in the time evolution of the average photon counts when stopping at the $5\pi/2$ time during Mølmer-Sørenson flopping and the RF power supplied to the can seem correlated without the RF lock. This suggests a common noise source causing these fluctuations.
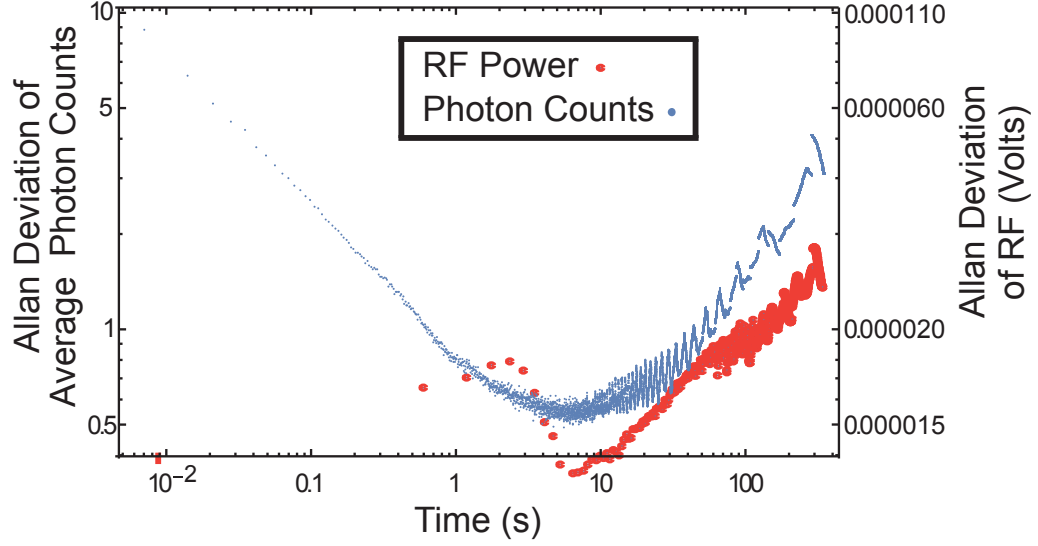
Figure 3.9: **Allan Deviation of the Average Photon Counts and RF voltage Without the RF Lock.** The Allan deviation begins to increase after the same time period for both the average photon counts when stopping at the $5\pi/2$ time during Mølmer-Sørenson flopping and the RF power supplied to the can. This futher suggests that both of these quantities are limited by the same noise source.

for the average photon counts with two ions when stopping at the $5\pi/2$ time during Mølmer-Sørenson flopping and the RF supplied to the can both diverge at the same time scale suggesting a common noise source.

The RF power is stabilized by locking the aforementioned measured rectifier voltage to a set point using a PID (New Focus LB1005 High-Speed Servo Controller) and feeding back to a mixer which is being used as a voltage controlled attenuator as seen in Figure 3.7. After locking the RF power to the can one can see increased stability of both the RF power and the Mølmer-Sørenson flopping frequency in that the Allan deviation in Figure 3.10 continues to average down for larger values of
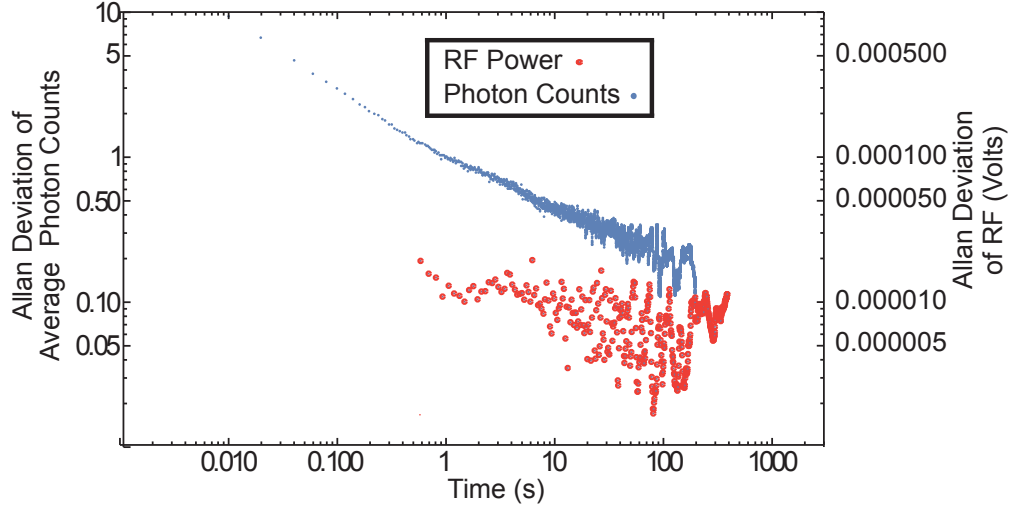
Figure 3.10: **Allan Deviation of the Average Photon Counts and RF Voltage with the RF Lock.** Application of the lock of the RF supplied to the can results in a decrease of the Allan deviation of the average photon counts when stopping at the $5\pi/2$ time during Mølmer-Sørenson flopping and the RF supplied to the can over a significantly longer time period than without the lock. This seems to indicate, that stabilizing the RF power delivered to the can increases the stability of the spin-spin interactions.

τ than when it was not locked. It is also evident from Figure 3.11 that although the fluctuations between the RF power and average photon counts still have some correlation, there are different sources driving the fluctuations in each case as they are not as correlated as when the lock was not engaged.

In the future we may stop locking Ω_T to the can resonance and directly sample and lock the RF voltage on the high voltage side of the can using a capacitive divider [50]. This will result in a more stable value of ω_{trap} because even though
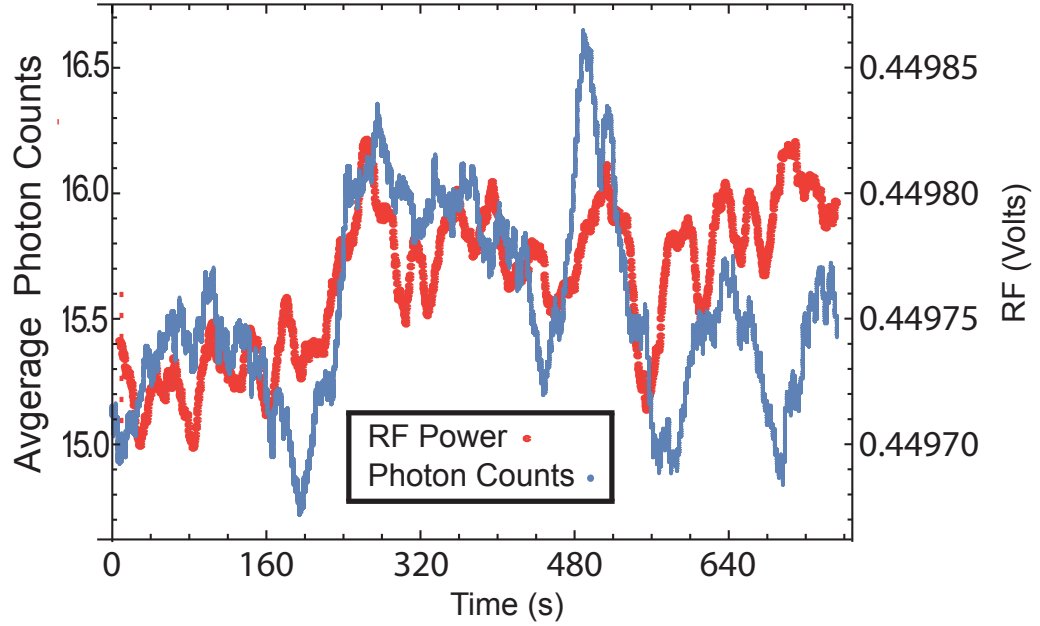
Figure 3.11: **Average Photon Counts and RF Voltage vs Time with the RF Lock.** After locking, there are smaller flucuations in the time evolution of the average photon counts when stopping at the $5\pi/2$ time during Mølmer-Sørenson flopping and the RF power supplied to the can. These flucuations in these two quantities seem to be less correlated than without the lock on the RF supplied to the can which seems to indicate that their stability is limited by different noise sources.

the current locking scheme keeps a constant RF voltage applied to the can, changes in Ω_T due to shifts in the can resonance destabilize the power delivered to the trap and ω_{trap}. Whereas stabilizing the RF voltage on the high voltage side of the can will result in a stable value of $\frac{V_0}{\Omega_T}$, and thus a stable ω_{trap}.

3.5   Random Anecdotal Evidence to Achieve Longer Lifetimes

In the past year or so we have been experiencing much longer ion lifetimes. We have been doing a few things a little bit differently that seem to have improved this, but we have never systemically studied it. I will present this anecdotal evidence here.

The factor that seems to have the most significant impact is the 935 nm light frequency and power. The power coupled into the 935 nm fiber drifts, and we find optimizing this fiber coupling and, thus, delivering more 935 nm power to the ions increases lifetimes. In addition, over the course of the day the wavemeter drifts and when this happens its calibration is no longer valid. Sometimes this drift can be rather substantial and we seem to have improved lifetimes if we optimize the 935 nm every couple of hours or after one of the labs recalibrates the wavemeter. We optimize the 935 nm frequency by aligning it for maximum detection florescence with 10 ions. It seems that the enhanced sensitivity of doing this optimization with 10 ions instead of 1 improves the ion lifetimes.

Our theory of why we see longer lifetimes with better D state repumping is that we are better able to cool the ions. Thus, when there is a less energetic collision

between a background gas molecule and the ion chain we are quickly able to re-cool it before it melts the ion chain. Similarly, we see seemingly longer lifetimes when sideband and Doppler cooling are optimized. In addition, to further improve the efficiency of ion cooling we have an another Doppler cooling beam that is further detuned from resonance by the RF drive frequency in an attempt to cool ions that are experiencing micromotion. This additional Doppler cooling beam seems to substantially improve cooling of the ions during loading when the RF drive to the trap is low.

We also see that sometimes ions become trapped in higher energy orbits where a 1-D chain will crystallize and there will still be another ion trapped that will collide with the 1-D chain and reduce the lifetimes. This seems to happen in two cases: loading and after recrystalization. Sometimes when the RF is low during loading we will crystalize the desired number of ions, but there will still be an additional ion in a higher energy orbit. To prevent this, one should wait about 15 seconds after the desired number of ions has crystalized to ensure that another ion is not in the trap (another additional ion will crystalize during this time if it is in the trap). If one does not wait this extra time, occasionally the ion chain will melt quickly after the trap RF has returned to its normal operating value, presumably due to a collision between the ions in the 1-D chain and the ion that was in a higher energy orbit.

Often after a collision melts the ion chain and we lower the trap RF we do not recrystalize all of the ions. In this case, if one keeps the recrystalized ions and loads back up to the desired number of ions, the ensuing chain lifetime will sometimes be brief. To prevent this, one should always turn off the RF to the trap to eject the

ions and load from zero ions after a collision when all of the ions are not recaptured.

Chapter 4:   Many-Body Localiztion

4.1   Introduction

It is exceedingly rare in nature for systems to localize, or retain local information about their initial conditions at long times. In an important counterexample, Anderson demonstrated that localization can arise due to the presence of disorder, which can destructively scatter propagating waves and prevent transport of energy or particles [1]. Although this interference effect can be applied to generic quantum systems, most experimental work has been restricted to the narrow parameter regime of low excitation energies and no interparticle interactions [6–8].

Whether such localization persists in the more general case of arbitrary excitation energy and non-zero interparticle interactions was theoretically explored by Anderson [1], and more recently by others [2,3,66–68]. This MBL phase is predicted to emerge for a broad set of interaction ranges and disorder strengths, though the precise phase diagram is not well known [41] since equilibrium statistical mechanics breaks down in the MBL phase and numerical simulations are limited to ~ 20 particles [66,67]. Experiments have measured constrained mass transport [21], the breakdown of ergodicity [10], the coupling of identical 1-D MBL systems [23], periodically driven MBL [12], and have mapped the 2-D MBL transition in disordered

atomic systems with interactions [22].

Here we report the direct observation of MBL in a long-range transverse field Ising model with programmable, random disorder. This is a non-integrable model that cannot be mapped to noninteracting particles (a necessary condition for MBL [3]) and we can easily tune the disorder strength and interaction range over a parameter space that exhibits this phenomenon. Our experiment is effectively a closed quantum system over the timescales of interest, since the system localizes approximately 60 times faster than the coupling rate to the outside environment.

The Hamiltonian for this investigation of MBL is given by:

$$H_{\text{Ising}} = \sum_{i<j} J_{i,j} \sigma_i^x \sigma_j^x + \frac{B}{2} \sum_i \sigma_i^z + \sum_i \frac{D_i}{2} \sigma_i^z \qquad (4.1)$$

with the origin of the spin-spin coupling and transverse field discussed above. The site-specific programmable disorder term D_i is sampled from a uniform random distribution with $D_i \in [-W, W]$. The disorder is generated by site-dependent laser-induced Stark shifts discussed in a previous chapter.

4.2   Measuring the Spin-Spin Coupling Matrix

For our study of MBL, we tune α between 0.95 and 1.81, although for most of the data $\alpha \approx 1.13$. We directly measure the complete spin-spin coupling matrix (Fig. 4.1a) for $\alpha \approx 1.13$, demonstrating the long-range interactions required to exhibit MBL in this model. In order to observe the dynamics between just two of

the ions in the chain, we shelve the other spins out of the interaction space. This is done by performing a π rotation between $|\downarrow\rangle_z$, $^2S_{1/2}|F = 0, m_F = 0\rangle$, and one of the Zeeman states, $^2S_{1/2}|F = 1, m_F = -1\rangle$, while shifting the two ions of interest out of resonance by applying a large Stark shift with the individual addressing beam. We then apply our Hamiltonian which now acts only on the two ions left in the interaction space and determine the elements of the spin-spin coupling matrix by fitting the measured interaction Rabi flopping frequency between each pair of spins. We applied a Stark shift to all but two of the ions instead of applying a Stark shift to just two of the ions because it is less susceptible to cross talk. Since even if there is some unwanted Stark shift on one of the two ions of interest it will still be small compared to the intended stark shift on the other ions.

4.3 Arbitrary Product State Preparation

State initialization starts with optically pumping the spins with high-fidelity to $|\downarrow\downarrow\downarrow\cdots\rangle_z$. Then we perform a global $\pi/2$ rotation to bring the ions to $|\downarrow\downarrow\downarrow\cdots\rangle_x$. At this point we apply a Stark shift with the individual addressing beam to the spins that are to be flipped and allow the chain to evolve until these ions are π out of phase with rest of the ions. This, along with our ability to perform high fidelity global rotations, allows for the preparation of any arbitrary product state along any direction of the Bloch sphere. Individual spin flips can be achieved with a fidelity of ~ 0.97, while arbitrary state preparation can be done with a fidelity of $\sim (0.97)^N$, where N is the number of spins flipped with the individual addressing beam.
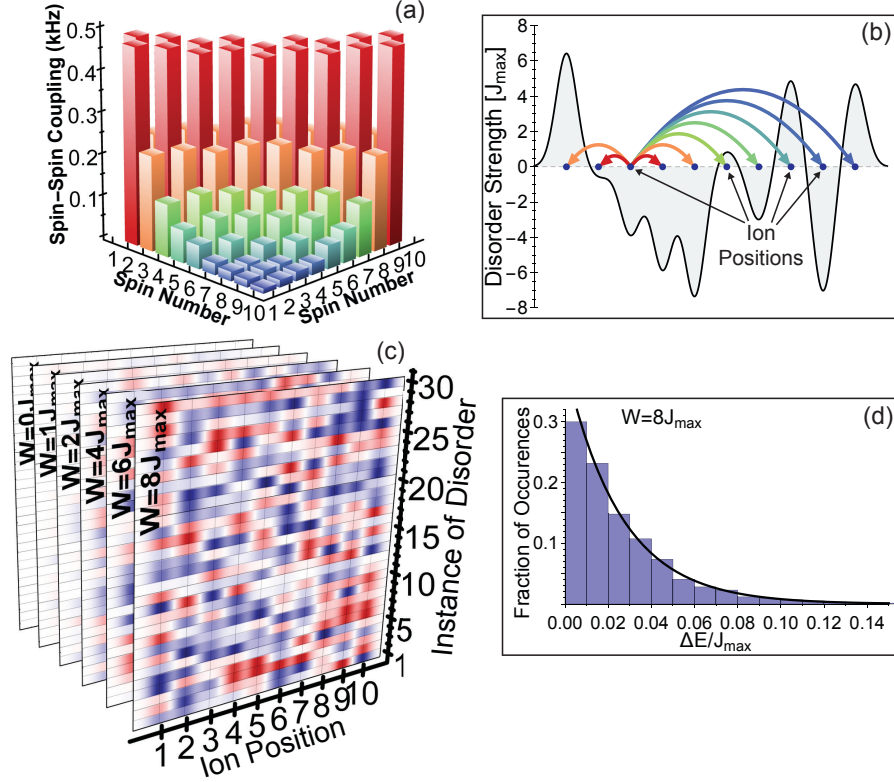
Figure 4.1: **An Interacting Spin Model with Random Disorder.** (a) Directly measured elements of the spin-spin coupling matrix J_{ij}, Eq. (4.1), (increasing interaction strength from blue to red). The long range interactions decay as $J_{max}/r^{1.13}$. (b) A specific instance of the random disordered field with a schematic illustration of the long-range interactions and (c) the random values of the disordered field for all 30 instances of disorder for several different disorder strengths and for each ion (red indicates positive values, and blue indicates negative values, with values between -0.5 and 0.5). (d) The level statistics calculated from the measured spin-spin coupling matrix (a) and applied disorders (c) are Poisson-distributed (black line is the expected level spacings for a Poisson distribution), as predicted for a MBL system.

We choose to study MBL with the Neél ordered initial state, $|\uparrow\downarrow\uparrow\downarrow\cdots\rangle_z$, because when $B \gg J$, the Hamiltonian is effectively an XY model [35, 36] and conserves $\sum_i \sigma_i^z$, because Ising processes that change the total spin projection along the large field are energetically forbidden. Thus, being in a spin configuration with half of the spins up and half of the spins down maximizes the accessible energy states. In addition, the Neél state is never an eigenstate, even for $B \gg J$ and $W \gg J$, since the uniform B field at each site still allows spin exchange in the z-basis.

4.4 Determining a Set of Thermalizing Parameters

Before searching for evidence of localization, we first find parameters that cause the measured state to thermalize in the absence of disorder. Figure 4.2 shows the time evolution of $\langle \sigma_i^x \rangle$ for different values of B for the spins initialized in the randomly chosen product state $|\downarrow\downarrow\downarrow\uparrow\downarrow\downarrow\downarrow\uparrow\downarrow\uparrow\rangle_x$. Without a transverse field, the spins are in an eigenstate of the Ising interaction and undergo no evolution. Once a transverse field is added the individual spins begin to lose memory of their initial conditions and as its strength is increased, the ions thermalize faster and more robustly.

To confirm the system is thermalizing, we measure the time evolution of the single site magnetization, $\langle \sigma_i^z \rangle$, along an orthogonal direction for different strengths of the transverse magnetic field starting with the spins initialized in the Néel ordered state. As seen in Fig. 4.2 the spins have lost information about their initial conditions

in the z direction for all values of B.

If a system is thermal, the Eigenstate Thermalization Hypothesis (ETH) provides a general framework where observables reach the value predicted by the microcanonical ensemble [69–71]. This allows us to calculate the expected thermal value of the reduced density matrix given the Hamiltonian and an initial state. To further establish that the system is thermalizing, we measure the reduced density matrix for each spin, $\rho_i =\mathrm{Tr}_{\{j\neq i\}}\rho$, without applied disorder and $B = 4J_{max}$ as shown in Fig. 4.3a. In our experiment, the spins are initially prepared in a product state with high fidelity. However at long times, the measured reduced density matrices show that each of the spins are very close to the zero magnetization mixed state, implying the system has locally thermalized.

An important signature of the MBL phase is manifested in the spectral statistics of adjacent energy levels of the Hamiltonian. In the thermalzing phase, the energy levels are given by the eigenvalues of a random-matrix, a matrix whose elements are given by a random distribution, due to level repulsion. However, in the MBL phase, this level repulsion is greatly suppressed since eigenstates typically differ by multiple spins flips. As a result, the level spacing between adjacent energy eigenvalues are Poisson-distributed [66, 67].

We calculate the spectral statistics of adjacent energy levels for the Hamiltonian and find they are not Poisson distributed for $B = 4J_{max}$ and $D_i = 0$ indicating that with no applied disorder, the system is not in a localized phase. Furthermore, one can determine if a system is in a thermal or localized regime by finding the correlation between adjacent energy splittings by calculating the ratio of two consecutive
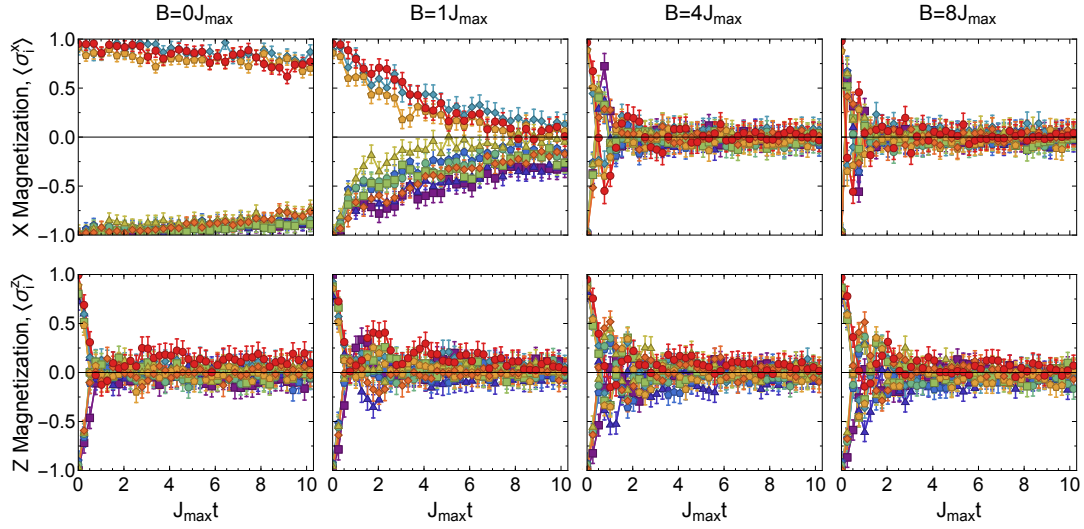
Figure 4.2: **Measured Thermalization in the Transverse Field Ising Model.**
The upper panels show the time dynamics of $\langle \sigma_i^x \rangle$ (different colors represent different ions) for 10 spins prepared in the random product state $|\downarrow\downarrow\downarrow\uparrow\downarrow\downarrow\downarrow\uparrow\downarrow\uparrow\rangle_x$, for different transverse magnetic field strengths. For $B = 0$ the spins are in a eigenstate and do not thermalize. However, as the strength of B is increased the system begins to thermalize more robustly and quickly. The lower panel plots the time evolution of $\langle \sigma_i^z \rangle$ with 10 spins prepared in the Néel ordered in the z direction for different transverse magnetic field strengths. We conclude that the system is in the thermalizing regime for $B = 4J_{max}$ since we observe thermalizing behavior along two orthogonal directions. Error bars are 1 standard deviation of statistical error.
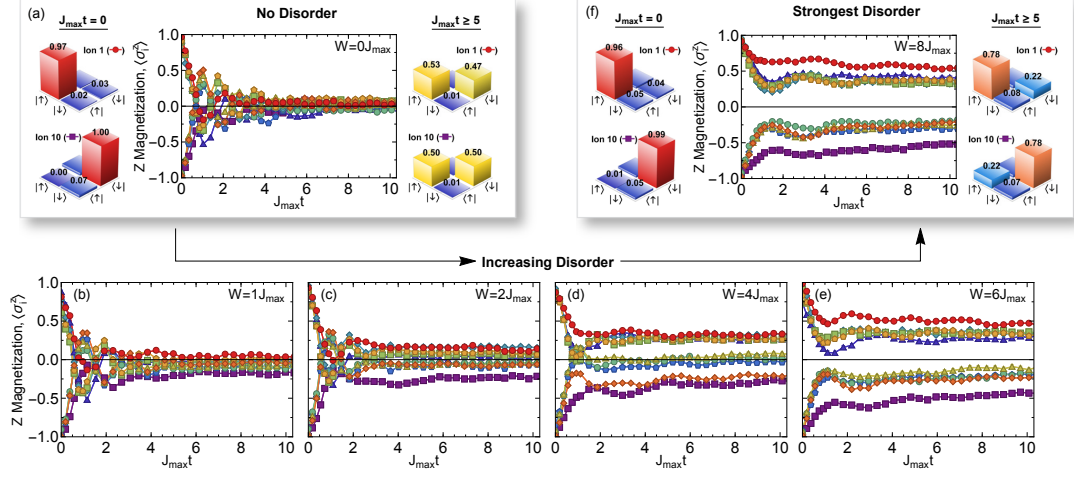
Figure 4.3: **Emergence of a Many-Body Localized State.** (a) shows the time-evolved single-site magnetizations $\langle \sigma_i^z \rangle$ (different colors represent different ions) for the Hamiltonian in Eq. (4.1) and with $B = 4J_{max}$ with no applied disorder ($D_i = 0$). The initial-state reduced density matrices for ions 1 and 10 show the spins start in a product state along the z direction. The time-averaged reduced density matrices for $J_{max}t > 5$ (colors from blue to red indicate increasing values of the elements of the density matrix) agree with the values predicted by the ETH, implying the system has thermalized locally. (b-e) As the disorder strength increases the spins retain more information about their initial state, indicating a transition towards MBL. (f) shows the dynamics of $\langle \sigma_i^z \rangle$ for the strongest applied disorder, $W = 8J_{max}$. The initial and steady-state time-averaged reduced density matrices for ions 1 and 10 now show that information is preserved about the initial spin configuration at the end of the evolution. Statistical error bars (1 s.d.) are smaller than the data points.

gaps [66]:

$$r_n = \frac{min\{\delta_n, \delta_{n-1}\}}{max\{\delta_n, \delta_{n-1}\}} \tag{4.2}$$

where $\delta_n = E_{n+1} - E_n \geq 0$. For a localized phase, where one expects a Poisson energy spectrum, the probability distribution of this order parameter is given by $P_p(r) = 2/(1 + r)^2$ and thus $\langle r \rangle \approx 0.39$. For energy level spacings following a random-matrix as predicted for a thermalizing regime, we calculate $\langle r \rangle \approx 0.53$ for a chain of 10 spins. Figure 4.4 shows that $\langle r \rangle$ saturates to the expected value for a random matrix distribution, indicating that the Hamiltonian is thermal for sufficiently large B.

In contrast to using our directly measured spin-spin couplings and applied realizations for the strongest experimental disorder $W = 8J_{max}$ and $B = 4J_{max}$, we calculate the distribution of adjacent energy level splittings and find them to be Poisson-distributed, as expected for a MBL state (Fig. 4.1d).

4.5 Calculating the Density Matrix Expected by the Eigenstate Thermalization Hypothesis

Given a Hamiltonian and an initial state $|\psi_0\rangle$, the corresponding energy is $\langle \psi_0 | H | \psi_0 \rangle$. For a thermalizing system satisfying ETH this energy should be equal to the classical energy:

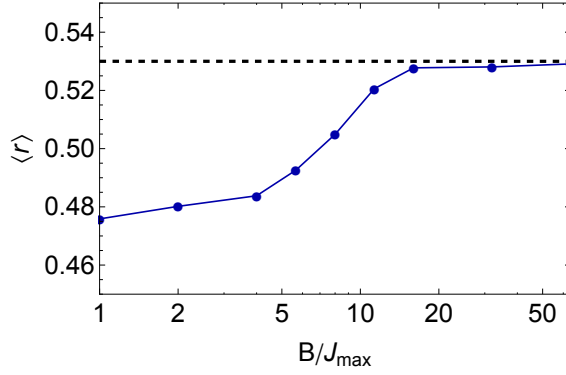$$E = \frac{\text{Tr}[H e^{-\beta H}]}{\text{Tr}[e^{-\beta H}]} \tag{4.3}$$

Figure 4.4: **Thermalizing Level Statistics.** The calculated value of $\langle r \rangle$ with respect to B saturates close to the predicted value for a random-matrix distribution (dashed black line) implying that the Hamiltonian is in the thermal phase for sufficiently large B.

for the appropriate $\beta = 1/(k_B T)$. When partitioning the entire system into subsystems A and B, with the size of A much smaller than B (perhaps even a single spin), then, the density matrix on site A at long times can be approximated by:

$$\rho_A = \frac{\text{Tr}_\text{B}[e^{-\beta H}]}{\text{Tr}[e^{-\beta H}]} \tag{4.4}$$

Since we start in the Néel ordered state, the initial energy given the Hamiltonian in Eq. (4.1) is equal to zero, $\langle \psi_0 | H | \psi_0 \rangle = 0$. Equating this to the right hand side of Eq. (4.3) and solving for β gives $\beta = 0$, or $T = \infty$. Using this β in Eq. (4.4) gives a value for any reduced thermal density matrix of:

$$
\begin{pmatrix}
1/2 & 0 \\
0 & 1/2
\end{pmatrix}
$$

in agreement with the measured reduced density matrices in Fig. 2a.

4.6   Initial State Memory Retention

We apply the random disordered potential, $D_i \neq 0$, with $B = 4J_{max}$ and observe the emergence of MBL as we increase the strength of disorder. Since the many-body eigenstates in the MBL phase are not thermal, transport of energy and spins is suppressed, and ETH fails. Thus, observables will not relax to their thermal values [67] and memory of the initial conditions will be evident in the single-site magnetization. When starting in the Neél ordered state, Fig. 4.3b-f shows the time evolution of $\langle \sigma_i^z \rangle$ for different disorder strengths. The frozen moments of the spins increase with increasing disorder as the emergent integrals of motion become more strongly localized [68].

With the maximum applied disorder, $W = 8J_{max}$, we measure the single-spin reduced density matrix for the initial state and the averaged matrix for $J_{max}t \geq 5$. In this case, localization of the spins leads to a marked difference in the measured and thermal reduced density matrices, indicating memory of the system's initial conditions and a breakdown of ETH.

4.7 Normalized Hamming Distance Quantifies Localization

To quantify the localization, we measure the normalized Hamming distance (HD) [42]:

$$\mathcal{D}(t) = \frac{1}{2} - \frac{1}{2N} \sum_i \langle \psi_0 | \, \sigma_i^z(t) \sigma_i^z(0) \, | \psi_0 \rangle \tag{4.5}$$

which gives the number of spin flips away from the initial state, normalized by the length of the chain. At long times, the HD approaches 0.5 for a thermalizing state and remains at 0 for a fully localized state. In Fig. 4.5a, we measure that the long-time HD is 0.5 in the absence of disorder, and becomes smaller as the disorder strength is increased and the system more strongly localizes.

Figure 4.5b shows that for finite but weak disorder, the time-averaged HD for $J_{max}t > 5$ is essentially unchanged, indicating weak or no localization. However, once the random field is sufficiently strong we observe a crossover from a thermalizing to a localized state. Once in this regime, the system becomes more localized with increasing disorder strength.

4.8 Comparison to Numerics

To demonstrate the MBL we observe is a general feature of our Hamiltonian we perform numerical simulations using exact diagonalization. Figure 4.6 compares the experimentally measured time evolution of the normalized HD with numerics and
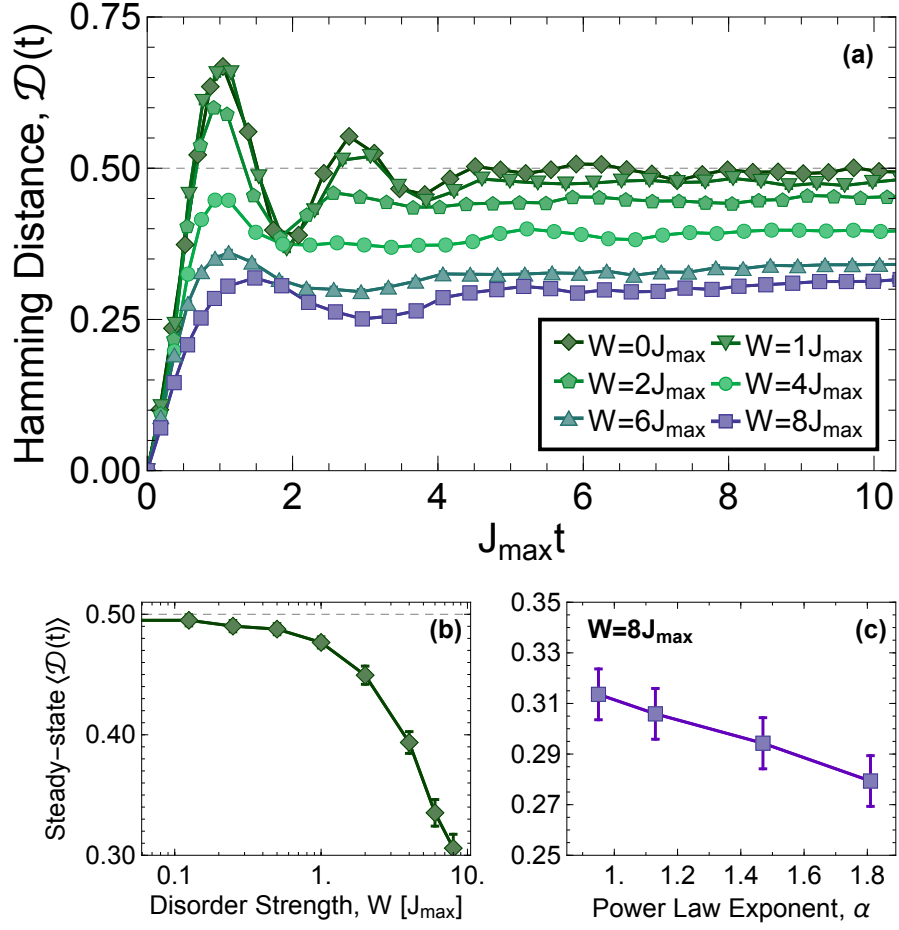
Figure 4.5: **Hamming Distance (HD).** (a) The Hamming Distance (HD) exhibits time dynamics that reach their steady-state values after $J_{max}t \approx 5$. For increasing disorder, the system becomes more strongly localized, and the steady-state Hamming Distance decreases. (different colors represent different disorder strengths). (b) The steady-state HD with respect to the strength of the random potential indicates the state is not or only weakly localized for small disorder, but after the random field is sufficiently strong it becomes more localized with increased disorder. (c) The system becomes less localized in the presence of longer-range interactions (smaller α). Error bars, 1 s.d.
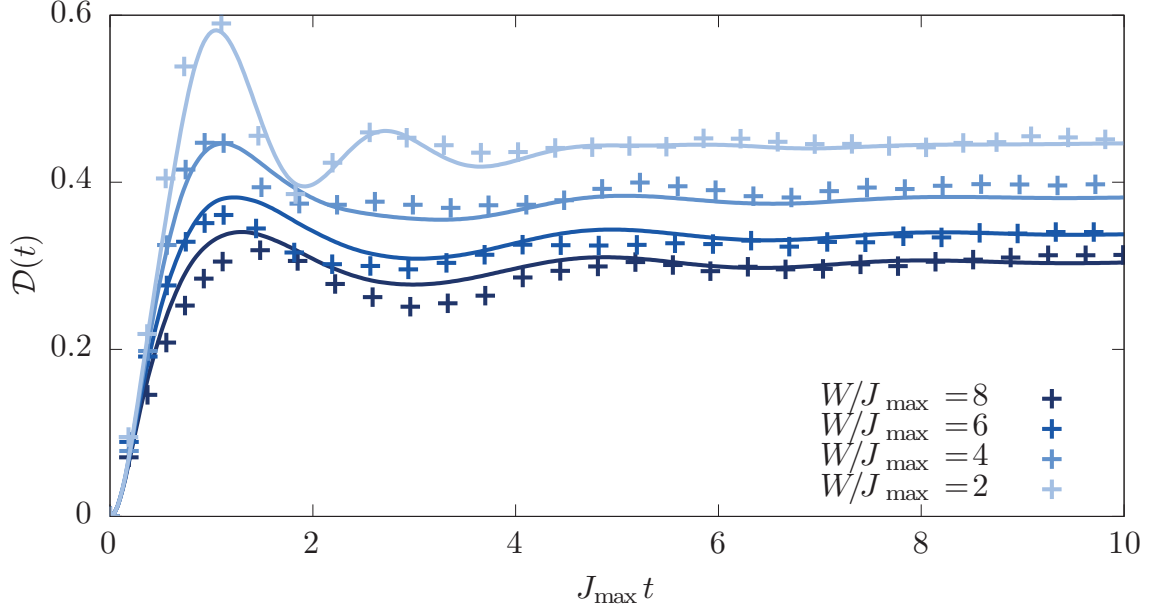
Figure 4.6: **Comparison of the Experimental Data (crosses) with Exact Numerical Simulations (blue lines) for Normalized Hamming Distance.** There is excellent agreement between the numerical simulations using the experimental parameters and the measured data. This demonstrates that the observed effects are general features of the Hamiltonian.

shows excellent agreement between them. We see similar agreement between experimental data and numerics for the time evolution of the single-spin magnetizations (not shown). The aspects of MBL we experimentally measure were independently verified numerically as generic characteristics of (4.1) [72].

4.9 Localization with Respect to Interaction Range

There is great theoretical interest in mapping the MBL phase diagram with respect to interaction range and disorder strength [41–43]. We have taken the first

steps towards this goal by measuring a change in the time-averaged HD for $W = 8J_{max}$ and $J_{max}t > 5$ as we adjusted the interaction range, $0.95 < \alpha < 1.81$ (Fig. 4.5c). For shorter-range interactions, the system appears more localized, since the state approaches a fully-localized Anderson insulator as $\alpha \to \infty$. This change in time-averaged HD with a change in interaction range makes clear that the long-range couplings are playing a role in the observed dynamics, thus indicating the observed effect is a many-body phenomenon.

Although there are predictions of a many-body delocalization transition at $\alpha = 1.5$ [43, 44], we did not observe this effect as we tuned α across this boundary. The lack of a sharp transition, along with the presence of MBL states for $\alpha < 1$, may be due to finite size effects. As this system is scaled to many dozens of spins, it will allow better study of the phase transition and mapping of the phase boundary in a regime where numerics are intractable.

4.10   Decoherence and Dephasing

To measure our system's coupling to the environment we fit an exponential decay to the dynamics in the upper left panel of Fig. 4.2 as we expect no time evolution of $\langle \sigma_i^x \rangle$ because the initial state is an eigenstate of the Hamiltonian and thus any dynamics give an estimate of the decoherence rate. We find this estimate to be $J_{Max}t = 64.6$ which is approximately 60 times slower than the dynamics of the localization.

Figure 4.7 shows a numerical simulation of the extended dynamics for the

model Hamiltonian with (green curves) and without (blue curves) crosstalk error between ions from the individual addressing and laser intensity noise on the Ising couplings. It is clear that the localization persists well beyond the experimental timescales even when accounting for experimental noise. We model the crosstalk noise on the disordered field by adding 5% of the Stark shift applied to adjacent ions to the size of the intended Stark shift which is consistent with the spillover we measure between ions. To incorporate noise on the spin-spin couplings, we scale the strength of the Ising couplings by a value we pull randomly from a Gaussian distribution centered around $\mu = 1$ with $\sigma = 0.05$ for each instance of disorder because the laser intensity noise is slower than the duration of an experiment. The size of this simulated noise is consistent with the directly measured noise on $J_{i,j}$.

4.11 Measuring Characteristic Growth of Entanglement with the Quantum Fisher Information

A hallmark of MBL is the characteristic growth of entanglement under coherent time evolution [73], though its experimental observation has been elusive so far. In Anderson insulators without many-body interactions, the entanglement production from weakly entangled initial states shows a quick saturation after a sharp transient regime. However, in MBL systems a long-time growth sets in, which is logarithmically slow for short-range interactions [74] and can become algebraic with power-law interactions [75].

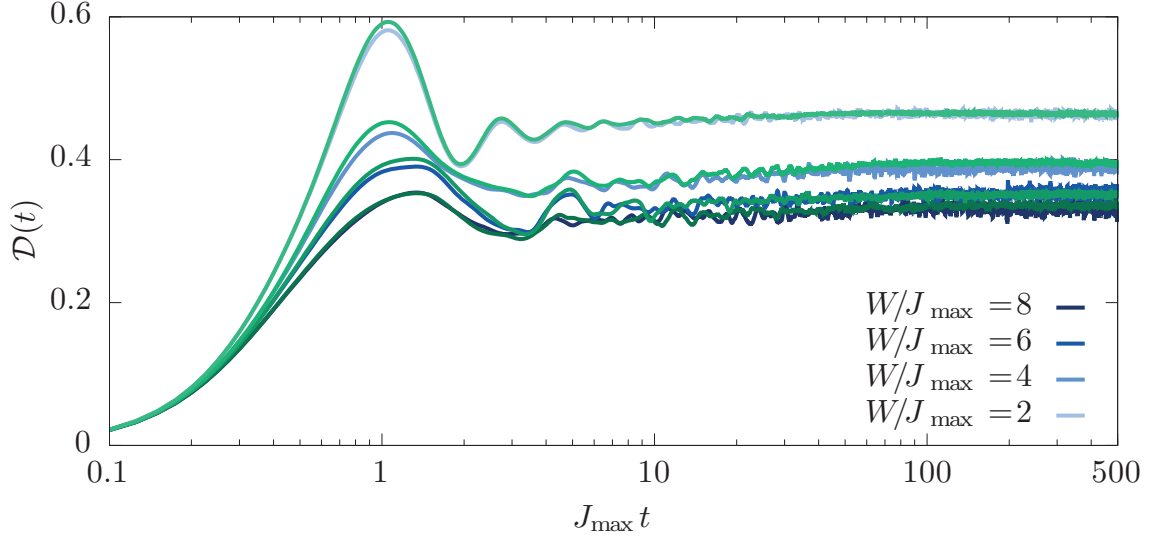This entanglement growth can be measured using a suitable witness operator

Figure 4.7: **Numerical Simulations of the Extended Time Evolution of the Hamming Distance for the Model Hamiltonian (blue curves) and with Experimental Noise (green curves).** The localization we observe persists much longer than the experimental timescale in the model Hamiltonian (blue curves) even when accounting for laser intensity noise and crosstalk between the ions from the individual addressing beam (green curves).

or even full state tomography [76]. We instead indirectly characterize the entanglement growth in this system by measuring the QFI [77–79]. The QFI has recently been shown to witness genuinely multipartite entanglement [80, 81]. From a quantum metrology perspective, the QFI quantifies the sensitivity of a given input state to a unitary transformation $e^{i\vartheta\hat{\mathcal{O}}}$ generated by the hermitian operator $\hat{\mathcal{O}}$. In a pure state, it is given by [78]:

$$F_Q = 4(\Delta\hat{\mathcal{O}})^2 = 4(\langle\hat{\mathcal{O}}^2\rangle - \langle\hat{\mathcal{O}}\rangle^2). \tag{4.6}$$

For a local operator $\hat{\mathcal{O}} = \sum_{i=1}^{N}\hat{\mathcal{O}}_i$ (where the difference between largest and smallest eigenvalue of $\hat{\mathcal{O}}_i$ is 1), the QFI witnesses entanglement as soon as:

$$f_Q \equiv F_Q/N > 1\,. \tag{4.7}$$

To characterize the growth of entanglement out of the initial Néel state, the natural choice of the generator $\hat{\mathcal{O}}$ is the staggered magnetization, $\hat{\mathcal{O}} = \sum_{i=1}^{N}(-1)^i\sigma_i^z/2$. Remarkably, this QFI is proportional to the variance of the HD $\mathcal{D}(t)$ given by (4.5):

$$F_Q = 4N^2(\Delta\hat{\mathcal{D}})^2 = \sum_{i,j}[(-1)^{i+j}\langle\sigma_i^z\sigma_j^z\rangle] - [\sum_i(-1)^i\langle\sigma_i^z\rangle]^2\,, \tag{4.8}$$

when associating $\mathcal{D}(t) = \langle\hat{\mathcal{D}}(t)\rangle$, with $\hat{\mathcal{D}} = 1/(2N)[1 - \sum_{i=1}^{N}(-1)^i\sigma_i^z]$.

With no applied disorder, we observe a fast initial growth of the QFI following
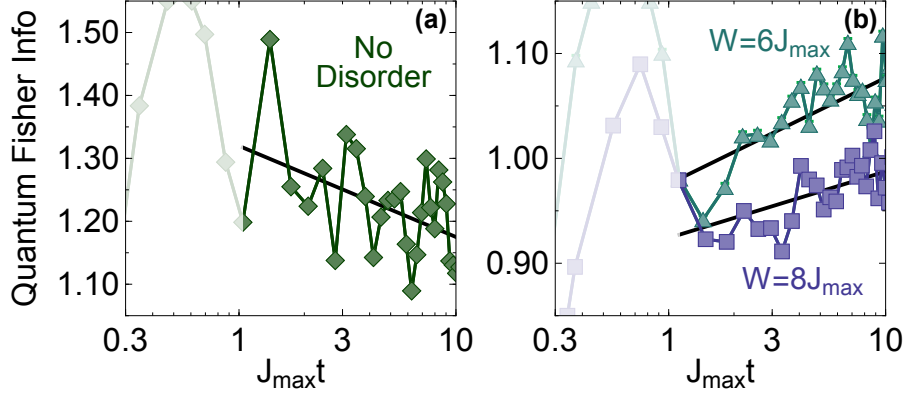
Figure 4.8: **Quantum Fisher Information (QFI).** (a) The time evolution of the QFI for no disorder which is consistent with no long-time growth of entanglement. The shaded area indicates the fast initial growth of QFI that follows a Lieb-Robinson-type bound. (b) The long-time logarithmic growth of the QFI for the applied disorder of $W = (6, 8)J_{max}$ is a lower bound for the entanglement in the system and is consistent with the expected long-time growth of entanglement in the MBL state. Black lines are logarithmic fits to the data. Statistical error bars (1 s.d.) are smaller than the data points.

a Lieb-Robinson bound [35, 36] as the correlations propagate through the system, but no further growth afterwards (Fig. 4.8a). In contrast, for the cases of applied disorder of $W = 6J_{max}$ and $W = 8J_{max}$, the further growth of the QFI is consistent with a logarithmic increase of entanglement at long times in a MBL state (Fig. 4.8b), but absent for single particle localized systems.

The QFI as defined in Eq. (4.6) assumes a pure state, i.e., that time evolution is purely unitary. For mixed states, the QFI cannot be expressed as a simple expectation value of the operator $\hat{\mathcal{O}}$ [78]. In general, decoherence reduces the purity
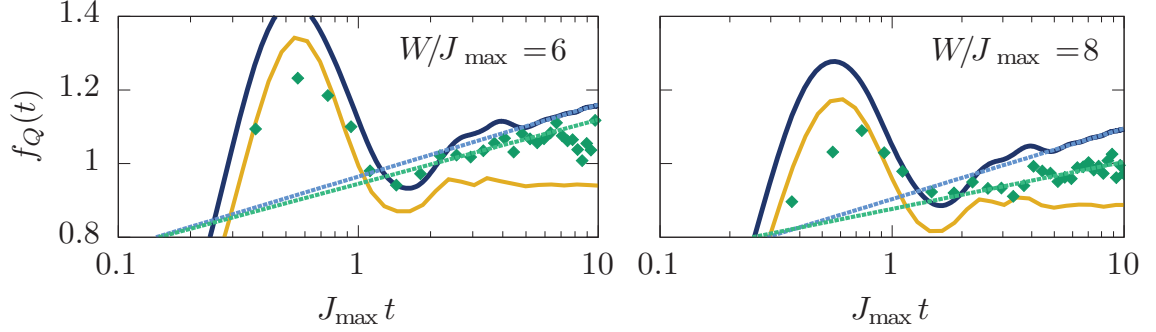
Figure 4.9: **Comparison of Experimental Data (green dots) with Exact Numerical Simulations for the Experimentally Applied Hamiltonian (thick blue lines) and Free-Fermion Theory (orange) for QFI.** The solid straight lines represent logarithmic fits to the numerical (light blue) and experimental data (light green). Deviations from the ideal coherent dynamics due to decoherence and other imperfections in the experimental setup, such as detection error, lead to a reduction of the QFI. Importantly, this suggests that experimental imperfections do not generate a false positive for entanglement. Moreover, there is long-time growth in the QFI from the measured data and applied Hamiltonian numerics that is absent in the free-fermion theory.

of the system's state over experimental time scales. To show that the measured increase of F_Q as defined in Eq. (4.8) is indeed due to coherent dynamics, we compare to numerical calculations for a unitary time evolution using the experimental parameters. Figure 4.9 shows the experimental data is always below the theoretical prediction for a unitary time evolution. The loss of purity or other experimental imperfections such as detection error, therefore, do not generate a false positive indicator of entanglement in our system.

Figure 4.10 further establishes this point, showing an increase in the QFI we measure and strong agreement between experimental data and theory when post-selecting for measured states with 5-spin excitations. We postselect because, as mentioned above, when $B \gg J$ the Hamiltonian is effectively an XY model and conserves $\sum_i \sigma_i^z$, because Ising processes that flip spins along the large field are energetically forbidden. However, because of camera detection error we find there is significant leakage out of states with 5-spin excitations ($\approx 70\%$ expected numerically, $\approx 35\%$ detected) into states with 4 and 6-spin excitations ($\approx 20\%$ detected) which should not be populated as the transverse magnetization is conserved modulo two spin flips in the transverse field Ising model. Thus, we post-select for states with 5-spin excitations. Figures 4.9 and 4.10 show a clear difference between the interacting case and a theory of free-fermions (see below) for the experimental data and numerical simulations, thus, establishing that the growth in QFI in the data and full-Hamiltonian numerics are due to a many-body effect.

To study how the localization changes with system size, we performed a numerical finite-size scaling. In order to obtain a well-behaved scaling, we use the Kac prescription [82], i.e., we adjust the couplings as $J_{ij} = J\mathcal{N}^{-1} |i - j|^{-\alpha}$, where $\mathcal{N} = (N-1)^{-1} \sum_{i<j} |i - j|^{-\alpha}$. Note that using this prescription the fundamental energy scale J differs by about a factor of 2 from J_{max}, the value used above.

For $\alpha > 2$, the disordered long-range Ising Hamiltonian shows MBL behavior at large disorder [83]. In Fig. 4.11, we plot the dynamics of the QFI for $\alpha = 3$, where it grows consistent with the characteristic long-time growth of entanglement for an MBL state. In particular, within a time window $2^\alpha < tJ < 3^\alpha$ where only
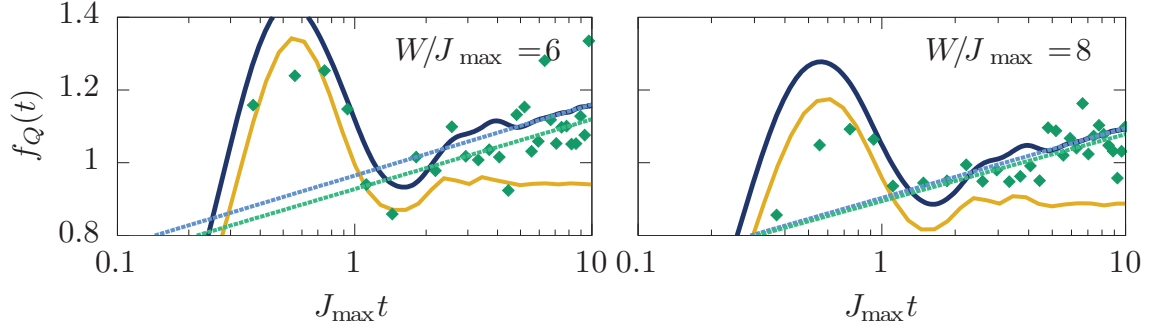
Figure 4.10: **Comparison of Postselected Experimental Data (green dots) with Exact Numerical Simulations for the Experimentally Applied Hamiltonian (thick blue lines) and Free-Fermion Theory (orange) for QFI.** The solid straight lines represent logarithmic fits to the numerical results for the experimentally applied Hamiltonian (light blue) and postselected data for results with 5 spin flips (light green). The increase in the postselected QFI and the agreement between the postselected data and numerical simulations supports the claim that experimental imperfections decrease the value of the QFI for the full experimental data.

next-nearest-neighbor interactions are relevant, the system essentially behaves as a nearest-neighbor Ising model with a weak next-to-nearest-neighbor coupling. For such a system, a logarithmic growth of entanglement is expected, as we indeed find in that regime, see inset in Fig. 4.11.

Moreover, in Fig. 4.11, we compare our numerical results to the appropriate long-range free-fermionic theory (see below), which shows a quick system-size independent saturation of the QFI without further growth. Therefore, we conclude that the observed increase of the QFI is not possible in a quantum system without many-body interactions, thus giving a clear signature for true MBL behavior.

The situation is more complex at $\alpha = 1.13$. For $B = 0$, it has been predicted that within the range $1 < \alpha < 2$ delocalized behavior could be expected in the thermodynamic limit [83]. As seen in Fig. 4.12, for the considered system sizes up to $N = 14$ the model displays all essential signatures of MBL, as found for $\alpha = 3$. However, the important question of whether this localization persists in the thermodynamic limit can only be addressed with system sizes larger than those accessible using exact diagonalization. Here, scaling our quantum simulator to larger system sizes could thus resolve a difficult open question, namely of the existence of ergodicity in the range $1 < \alpha < 2$. However, we would like to emphasize that the essential features of MBL are nevertheless captured by the 10-spin experimental system. In particular, we still find a time window consistent with a logarithmic growth of entanglement, see inset in Fig. 4.12.

In order to make a stronger connection between growth in the QFI and growth of entanglement we calculate the entropy of entanglement between two halves of the

chain:

$$S_A = -Tr[\rho_A \log \rho_A] \tag{4.9}$$

where $\rho_A = Tr_B[\rho]$ and B is the other half of the spin chain. The entanglement entropy quantifies the number of entangled bits between two subsystems.

In Figs. 4.11 and 4.12 it is clear that there is long-time growth of the entanglement entropy that is consistent with the expected growth for a MBL state [74, 75] and is absent in the free-fermion numerics. The difference between the numerics for the model Hamiltonian and the non-interacting theory for the QFI and the entanglement entropy in Figs. 4.13 and 4.14 distinguishes between the two cases for the experimental system size and timescale. These figures also establish a qualitative connection between growth in the QFI and growth in entanglement.

To show that the QFI growth is truly due to interactions, we also compare numerics with the experimentally applied Hamiltonian to a close approximation of H, Eq. (4.1), with a non-interacting theory. Using the Jordan-Wigner transformation, $\sigma_j^- \to e^{-i\theta_j} c_j$, with the phase of the string operator $\theta_j = \pi \sum_{j<i} c_j^\dagger c_j$, the Hamiltonian Eq. (4.1) can be mapped to a fermionic theory with annihilation and creation operators c_j and $c_j^\dagger$, respectively,

$$H = \sum_{i<j} J_{ij}(c_i^\dagger e^{i(\theta_j - \theta_i)} c_j + c_i^\dagger e^{i(\theta_j + \theta_i)} c_j^\dagger + h.c.) - \sum_i (B + D_i) c_i^\dagger c_i. \tag{4.10}$$

If J_{ij} contained only nearest-neighbor interactions, this Hamiltonian would become equivalent to a free-fermionic theory. For general J_{ij}, however, the string operators generate interactions between the fermions. Over short times, and especially in a localized regime, the phases θ_j are dominated by their initial values, i.e., it is a good
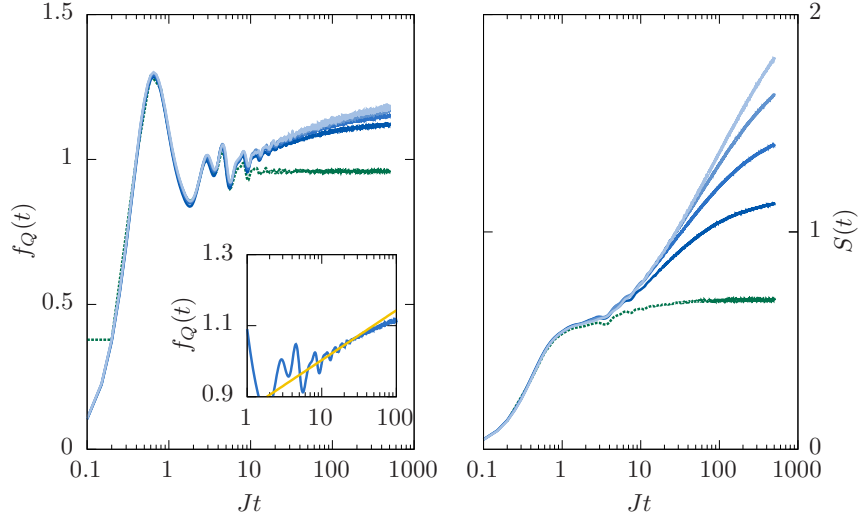
Figure 4.11: **QFI and Entanglement Entropy from Exact Diagonalization** $(\alpha = 3$ **and** $W/J = 8)$**.** Left panel: When subject to disorder, the QFI of the staggered magnetization shows a characteristic growth of entanglement (blue lines; from dark to light: $N = 8, 10, 12, 14$ averaged over $10^6, 3 \times 10^5, \ldots, 2500$ disorder realizations). This growth is absent in a theory of free-fermions with long-range hopping and pairing (green dashed lines with $N = 14$ (dark green) averaged over 10000 realizations). Left panel inset: In a time window dominated by next-nearest neighbor interactions, $2^\alpha < tJ < 3^\alpha$, one observes a characteristic logarithmic entanglement growth, expected for a MBL system with short-range interactions. Right panel: The entanglement entropy between two halves of the chain shows long-time logarithmic growth for the interacting case and saturates for the free-fermion theory consistent with the expectation for a MBL state and single-particle localized state, respectively, and a qualitative agreement between growth in QFI and entanglement entropy.
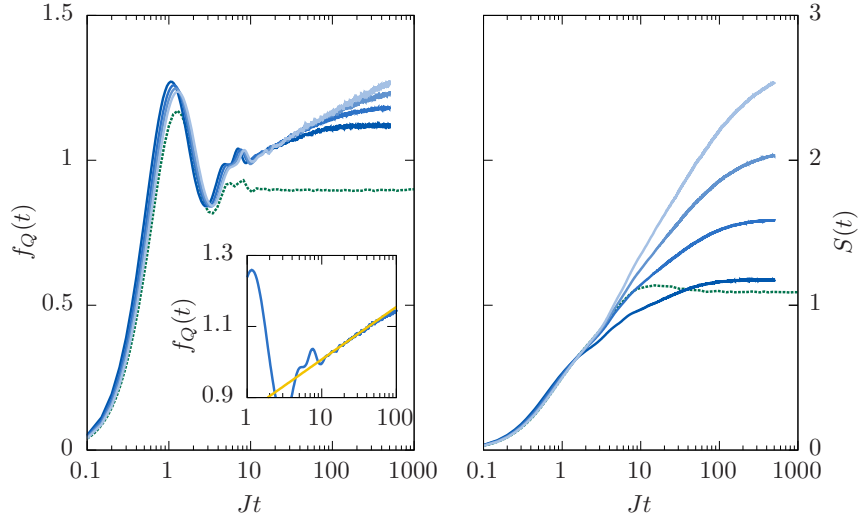
Figure 4.12: **QFI and Entanglement Entropy from Exact Diagonalization**
($\alpha = 1.13$ **and** $W/J = 8$**).** Same color coding as in Fig. 4.11. Importantly, for
the experimentally relevant system size of N = 10, we again find a time window
consistent with a logarithmic growth of entanglement in the growth of QFI (see left
inset) and half-chain entanglement entropy.

approximation to replace (for the initial Neel state) $\theta_j \to \pi \sum_{j<i}((-1)^j+1)/2$ in the Hamiltonian. This replacement amounts to approximating H by a non-interacting fermionic theory with long-range hopping and pairing. The QFI for that case is included in Figs. 4.11 and 4.12. As one can see, the QFI quickly saturates to values below $f_Q = 1$. The experimentally and numerically observed further growth of the QFI is thus truly due to interactions, and cannot be captured within a free-fermionic theory, even with long-range hopping.

4.12 Sampling Error

To ensure we observe the general behavior of the disordered Hamiltonian, we average 30 distinct random instances of disorder (Fig. 4.1b-c). We determine that averaging over 30 different random realizations of disorder is sufficient to have a sampling error smaller than the effect we observe by looking at the change in the time-averaged HD with respect to a change in the disorder strength. Figure 4.5b makes explicit that this error is much smaller than than the change in the time-averaged HD with respect to a change in the disorder strength.

Figure 4.13: **Difference between Numerics for the Interacting Model Hamiltonian and Free-Fermion Theory for QFI and Entanglement Entropy ($\alpha = 3$ and $W/J = 8$).** There is a clear departure between the numerically calculated QFI and entanglement entropy for the model Hamiltonian and the free-fermion theory.
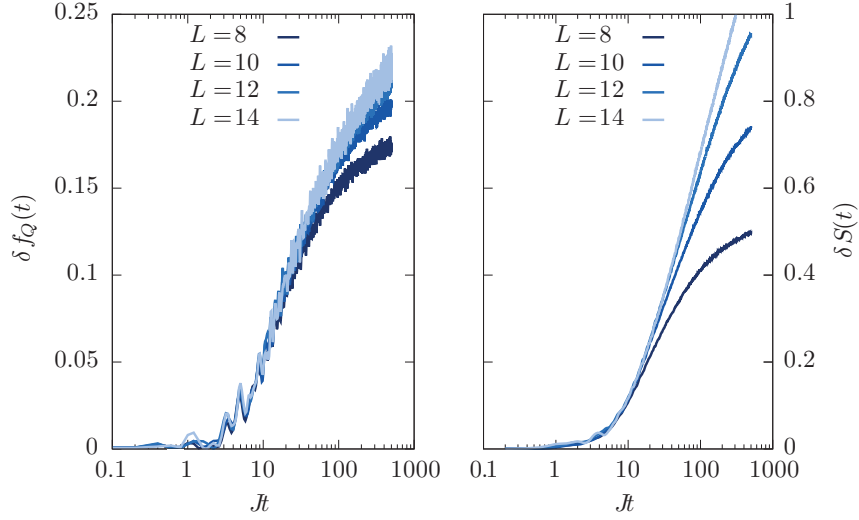
Figure 4.14: **Difference between Numerics for the Interacting Model Hamiltonian and Free-Fermion Theory for QFI and Entanglement Entropy ($\alpha = 1.13$ and $W/J = 8$).** There is a clear departure between the numerically calculated QFI and entanglement entropy for the model Hamiltonian and the free-fermion theory for N=10 on the experimental timescale.
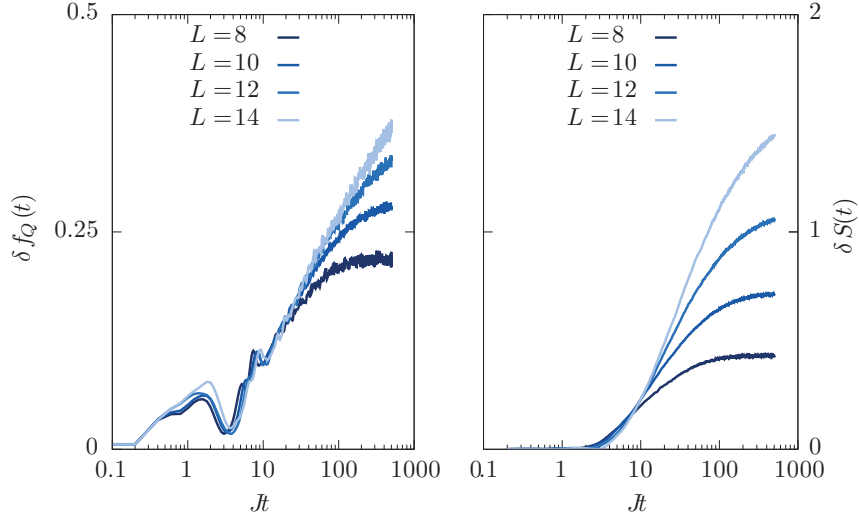
Bibliography

[1] P. W. Anderson, "Absence of diffusion in certain random lattices," *Phys. Rev.*, vol. 109, p. 1492, 1958.

[2] D. M. Basko, I. L. Aleiner, and B. L. Altshuler, "Metalinsulator transition in a weakly interacting many-electron system with localized single-particle states," *Ann. Phys.*, vol. 321, no. 5, pp. 1126–1205, 2006.

[3] D. M. Basko, I. L. Aleiner, and B. L. Altshuler, "Possible experimental manifestations of the many-body localization," *Phys. Rev. B*, vol. 76, p. 052203, 2007.

[4] T. Kinoshita, T. Wenger, and D. S. Weiss, "A quantum newton's cradle," *Nature*, vol. 440, p. 900, 2006.

[5] A. Polkovnikov, K. Sengupta, A. Silva, and M. Vengalattore, "Colloquium: Nonequilibrium dynamics of closed interacting quantum systems," *Rev. Mod. Phys.*, vol. 83, p. 863, 2011.

[6] D. S. Wiersma, P. Bartolini, A. Lagendijk, and R. Righini, "Localization of light in a disordered medium," *Nature*, vol. 390, p. 671, 1997.

[7] J. Billy, V. Josse, Z. Zuo, A. Bernard, B. Hambrecht, P. Lugan, D. Clément, L. Sanchez-Palencia, P. Bouyer, and A. Aspect, "Direct observation of anderson localization of matter waves in a controlled disorder," *Nature*, vol. 453, p. 891, 2008.

[8] G. Roati, C. D'Errico, L. Fallani, M. Fattori, C. Fort, M. Zaccanti, G. Modugno, M. Modugno, and M. Inguscio, "Anderson localization of a non-interacting bose-einstein condensate," *Nature*, vol. 453, p. 895, 2008.

[9] J. R. Garrison and T. Grover, "Does a single eigenstate encode the full hamiltonian?," *arXiv:1503.00729*, 2015.

[10] M. Schreiber, S. S. Hodgman, P. Bordia, H. P. Lschen, M. H. Fischer, R. Vosk, E. Altman, U. Schneider, and I. Bloch, "Observation of many-body localization of interacting fermions in a quasi-random optical lattice," *Science*, vol. 349, p. 842, 2015.

[11] J. Smith, A. Lee, P. Richerme, B. Neyenhuis, P. W. Hess, P. Hauke, M. Heyl, D. A. Huse, and C. Monroe, "Many-body localization in a quantum simulator with programmable random disorder," *Nat. Phys.*, vol. advance online publication, doi:10.1038/nphys3783, 2016.

[12] P. Bordia, H. Lschen, U. Schneider, M. Knap, and I. Bloch, "Periodically driving a many-body localized quantum system," *arXiv:1607.07868*, 2016.

[13] J. Berges, S. Borsányi, and C. Wetterich, "Prethermalization," *Phys. Rev. Lett.*, vol. 93, p. 142002, Sep 2004.

[14] M. Gring, M. Kuhnert, T. Langen, T. Kitagawa, B. Rauer, M. Schreitl, I. Mazets, D. A. Smith, E. Demler, and J. Schmiedmayer, "Relaxation and prethermalization in an isolated quantum system," *Science*, vol. 337, p. 1318, 2012.

[15] Z.-X. Gong and L.-M. Duan, "Prethermalization and dynamic phase transition in an isolated trapped ion spin chain," *New J. Phys.*, vol. 15, p. 113051, 2013.

[16] T. Langen, S. Erne, R. Geiger, B. Rauer, T. Schweigler, M. Kuhnert, W. Rohringer, I. E. Mazets, T. Gasenzer, and J. Schmiedmayer, "Experimental observation of a generalized gibbs ensemble," *Science*, vol. 348, no. 6231, pp. 207–211, 2015.

[17] I. B. Spielman, "Assembling a complex quantum ensemble," *Science*, vol. 348, no. 6231, pp. 185–186, 2015.

[18] I. Bloch, J. Dalibard, and S. Nascimbene, "Quanum simulations with ultracold gases," *Nat. Phys.*, vol. 8, p. 267, 2012.

[19] R. Blatt and C. F. Roos, "Quantum simulations with trapped ions," *Nat. Phys.*, vol. 8, p. 277, 2012.

[20] S. S. Kondov, W. R. McGehee, J. J. Zirbel, and B. DeMarco, "Three-dimensional anderson localization of ultracold matter," *Science*, vol. 334, p. 66, 2011.

[21] S. Kondov, W. McGehee, W. Xu, and B. DeMarco, "Disorder-induced localization in a strongly correlated atomic hubbard gas," *Phys. Rev. Lett.*, vol. 114, p. 083002, 2015.

[22] J.-y. Choi, S. Hild, J. Zeiher, P. Schauß, A. Rubio-Abadal, T. Yefsah, V. Khemani, D. A. Huse, I. Bloch, and C. Gross, "Exploring the many-body localization transition in two dimensions," *Science*, vol. 352, no. 6293, pp. 1547–1552, 2016.

[23] P. Bordia, H. P. Lüschen, S. S. Hodgman, M. Schreiber, I. Bloch, and U. Schneider, "Coupling identical one-dimensional many-body localized systems," *Phys. Rev. Lett.*, vol. 116, p. 140401, Apr 2016.

[24] A. M. Kaufman, M. E. Tai, A. Lukin, M. Rispoli, R. Schittko, P. M. Preiss, and M. Greiner, "Quantum thermalization through entanglement in an isolated many-body system," *arXiv:1603.04409*, 2016.

[25] B. Neyenhuis, J. Smith, A. C. Lee, J. Zhang, P. Richerme, P. W. Hess, Z.-X. Gong, A. V. Gorshkov, and C. Monroe, "Observation of prethermalization in long-range interacting spin chains," *arXiv:1608.00681*, 2016.

[26] K. Kim, M. S. Chang, R. Islam, S. Korenblit, L.-M. Duan, and C. Monroe, "Entanglement and tunable spin-spin couplings between trapped ions using multiple transverse modes," *Phys. Rev. Lett.*, vol. 103, p. 120502, 2009.

[27] K. Kim, M. S. Chang, S. Korenblit, R. Islam, E. E. Edwards, J. K. Freericks, G. D. Lin, L. M. Duan, and C. Monroe, "Quantum simulation of frustrated ising spins with trapped ions," *Nature*, vol. 465, p. 590, 2010.

[28] E. E. Edwards, S. Korenblit, K. Kim, R. Islam, M. S. Chang, J. K. Freericks, G. D. Lin, L. M. Duan, and C. Monroe, "Quantum simulation and phase diagram of the transverse-field ising model with three atomic spins," *Phys. Rev. B*, vol. 82, p. 060412, 2010.

[29] R. Islam, E. E. Edwards, K. Kim, S. Korenblit, C. Noh, H. Carmichael, G. D. Lin, L. M. Duan, C. C. J. Wang, J. K. Freericks, and C. Monroe, "Onset of a quantum phase transition with a trapped ion quantum simulator," *Nature Communications*, vol. 2, p. 377, 2011.

[30] B. P. Lanyon, C. Hempel, D. Nigg, M. Müller, R. Gerritsma, F. Zähringer, P. Schindler, J. T. Barreiro, M. Rambach, G. Kirchmair, M. Hennrich, P. Zoller, R. Blatt, and C. F. Roos, "Universal digital quantum simulation with trapped ions," *Science*, vol. 334, p. 57, 2011.

[31] S. Korenblit, D. Kafri, W. C. Campbell, R. Islam, E. E. Edwards, Z.-X. Gong, G.-D. Lin, L.-M. Duan, J. Kim, K. Kim, and C. Monroe, "Quantum simulation of spin models on an arbitrary lattice with trapped ions," *New J. Phys.*, vol. 14, no. 9, p. 095024, 2012.

[32] R. Islam, C. Senko, W. C. Campbell, S. Korenblit, J. Smith, A. Lee, E. E. Edwards, C. C. J. Wang, J. K. Freericks, and C. Monroe, "Emergence and frustration of magnetic order with variable-range interactions in a trapped ion quantum simulator," *Science*, vol. 340, p. 583, 2013.

[33] P. Richerme, C. Senko, J. Smith, A. Lee, and C. Monroe, "Experimental performance of a quantum simulator: Optimizing adiabatic evolution and identifying many-body ground states," *Phys. Rev. A*, vol. 88, p. 012334, 2013.

[34] P. Richerme, C. Senko, S. Korenblit, J. Smith, A. Lee, R. Islam, W. C. Campbell, and C. Monroe, "Quantum catalysis of magnetic phase transitions in a quantum simulator," *Phys. Rev. Lett.*, vol. 111, p. 100506, 2013.

[35] P. Richerme, Z.-X. Gong, A. Lee, C. Senko, J. Smith, M. Foss-Feig, S. Michalakis, A. V. Gorshkov, and C. Monroe, "Non-local propagation of correlations in quantum systems with long-range interactions," *Nature*, vol. 511, p. 198, 2014.

[36] P. Jurcevic, B. P. Lanyon, P. Hauke, C. Hempel, P. Zoller, R. Blatt, and C. F. Roos, "Quasiparticle engineering and entanglement propagation in a quantum many-body system," *Nature*, vol. 511, p. 202, 2014.

[37] C. Senko, J. Smith, P. Richerme, A. Lee, W. C. Campbell, and C. Monroe, "Coherent imaging spectroscopy of a quantum many-body spin system," *Science*, vol. 345, p. 430, 2014.

[38] C. Senko, P. Richerme, J. Smith, A. Lee, I. Cohen, A. Retzker, and C. Monroe, "Realization of a quantum integer-spin chain with controllable interactions," *Phys. Rev. X*, vol. 5, p. 021026, Jun 2015.

[39] K. Mølmer and A. Sørensen, "Multiparticle entanglement of hot trapped ions," *Phys. Rev. Lett.*, vol. 82, p. 1835, 1999.

[40] D. Porras and J. I. Cirac, "Effective quantum spin systems with trapped ions," *Phys. Rev. Lett.*, vol. 92, p. 207901, 2004.

[41] N. Yao, C. Laumann, S. Gopalakrishnan, M. Knap, M. Müller, E. Demler, and M. Lukin, "Many-body localization in dipolar systems," *Phys. Rev. Lett.*, vol. 113, p. 243002, 2014.

[42] P. Hauke and M. Heyl, "Many-body localization and quantum ergodicity in disordered long-range ising models," *Phys. Rev. B*, vol. 92, p. 134204, 2015.

[43] A. L. Burin, "Localization in a random xy model with long-range interactions: Intermediate case between single-particle and many-body problems," *Phys. Rev. B*, vol. 92, p. 104428, 2015.

[44] C. R. Laumann and N. Y. Yao, "Statistical physics: Localization goes long," *Nat. Phys.*, vol. advance online publication, doi:10.1038/nphys3854, 2016.

[45] A. C. Lee, J. Smith, P. Richerme, B. Neyenhuis, P. W. Hess, J. Zhang, and C. Monroe, "Engineering large stark shifts for individual full control of clock state qubits," *arXiv:1604.08840*, 2016.

[46] R. Islam, *Quantum Simulation of Interacting Spin Models with Trapped Ions.* PhD thesis, University of Maryland, College Park, 2012.

[47] S. Korenblit, *Quantum Simulation of the Ising Model with Trapped Ions: Devil's Staircase and Arbitrary Lattice Proposal.* PhD thesis, University of Maryland, College Park, 2013.

[48] C. Senko, *Dynamics and Excited States of Quantum Many-Body Spin Chains with Trapped Ions.* PhD thesis, University of Maryland, College Park, 2014.

[49] A. C. Lee, *Engineering a Quantum Many-Body Hamiltonian with Trapped Ions.* PhD thesis, University of Maryland, College Park, 2016.

[50] K. G. Johnson, J. D. Wong-Campos, A. Restelli, K. A. Landsman, B. Neyenhuis, J. Mizrahi, and C. Monroe, "Active stabilization of ion trap radiofrequency potentials," *Rev. Sci. Instrum.*, vol. 87, no. 5, p. 053110, 2016.

[51] D. F. James and J. Jerke, "Effective hamiltonian theory and its applications in quantum information," *Can. J. Phys.*, vol. 85, no. 6, pp. 625–632, 2007.

[52] H. Metcalf and P. van der Straten, *Laser Cooling and Trapping.* Springer, 1999.

[53] R. Zare, *Angular Momentum: Understanding Spatial Aspects in Chemistry and Physics.* Wiley-Interscience, 1988.

[54] J. A. Mizrahi, *Ultrafast Control of Spin and Motion in Trapped Ions.* PhD thesis, University of Maryland, College Park, 2013.

[55] D. J. Wineland, C. Monroe, W. M. Itano, D. Leibfried, B. E. King, and D. M. Meekhof, "Experimental issues in coherent quantum-state manipulation of trapped atomic ions," *Journal of Research of the National Institute of Standards and Technology*, vol. 103, p. 259, 1998.

[56] E. T. Jaynes and F. W. Cummings, "Comparison of quantum and semiclassical radiation theories with application to the beam maser," *Proc. IEEE*, vol. 51, p. 89, 1963.

[57] D. F. V. James, "Quantum dynamics of cold trapped ions with application to quantum computation," *Appl. Phys. B*, vol. 66, p. 181, 1998.

[58] S.-L. Zhu, C. Monroe, and L.-M. Duan, "Trapped ion quantum computation with transverse phonon modes," *Phys. Rev. Lett.*, vol. 97, p. 050505, 2006.

[59] G. Gabrielse, X. Fei, L. A. Orozco, R. L. Tjoelker, J. Haas, H. Kalinowsky, T. A. Trainor, and W. Kells, "Thosandfold improvement in the measured antiproton mass," *Phys. Rev. Lett.*, vol. 65, p. 1317, 1990.

[60] A. Chew, "Doppler-free spectroscopy of iodine at 739 nm," Master's thesis, University of Michigan, Ann Arbor, 2008.

[61] A. C. Lee, "Ytterbium ion qubit state detection on an iccd camera," Master's thesis, University of Maryland, College Park, 2012.

[62] S. Olmschenk, *Quantum Teleportation Between Distant Matter Qubits.* PhD thesis, University of Michigan, 2009.

[63] R. Islam, W. C. Campbell, T. Choi, S. M. Clark, C. W. S. Conover, S. Debnath, E. E. Edwards, B. Fields, D. Hayes, D. Hucul, I. V. Inlek, K. G. Johnson, S. Korenblit, A. Lee, K. W. Lee, T. A. Manning, D. N. Matsukevich, J. Mizrahi, Q. Quraishi, C. Senko, J. Smith, and C. Monroe, "Beat note stabilization of mode-locked lasers for quantum information processing," *Opt. Lett.*, vol. 39, pp. 3238–3241, 2014.

[64] D. W. Allan, "Statistics of atomic frequency standards," *Proc. IEEE*, vol. 54, pp. 221–230, Feb 1966.

[65] D. W. Allan, N. Ashby, and C. C. Hodge, *The Science of Timekeeping.* Hewlett Packard, 1997.

[66] V. Oganesyan and D. A. Huse, "Localization of interacting fermions at high temperature," *Phys. Rev. B*, vol. 75, p. 155111, 2007.

[67] A. Pal and D. A. Huse, "Many-body localization phase transition," *Phys. Rev. B*, vol. 82, p. 174411, 2010.

[68] M. Serbyn, Z. Papić, and D. A. Abanin, "Local conservation laws and the structure of the many-body localized states," *Phys. Rev. Lett.*, vol. 111, p. 127201, 2013.

[69] J. M. Deutsch, "Quantum statistical mechanics in a closed system," *Phys. Rev. A*, vol. 43, p. 2046, 1991.

[70] M. Srednicki, "Chaos and quantum thermalization," *Phys. Rev. E*, vol. 50, p. 888, 1994.

[71] M. Rigol, V. Dunjko, and M. Olshanii, "Thermalization and its mechanism for generic isolated quantum systems," *Nature*, vol. 452, p. 854, 2008.

[72] Y.-L. Wu and S. Das Sarma, "Understanding analog quantum simulation dynamics in coupled ion-trap qubits," *Phys. Rev. A*, vol. 93, p. 022332, Feb 2016.

[73] R. Nandkishore and D. A. Huse, "Many body localization and thermalization in quantum statistical mechanics," *Annu. Rev. Condens. Matter Phys.*, vol. 6, p. 15, 2015.

[74] J. H. Bardarson, F. Pollmann, and J. E. Moore, "Unbounded growth of entanglement in models of many-body localization," *Phys. Rev. Lett.*, vol. 109, p. 017202, 2012.

[75] M. Pino, "Entanglement growth in many-body localized systems with long-range interactions," *Phys. Rev. B*, vol. 90, p. 174204, 2014.

[76] H. Haeffner, W. Haensel, C. F. Roos, J. Benhelm, D. C. al kar, M. Chwalla, T. Koerber, U. D. Rapol, M. Riebe, P. O. Schmidt, C. Becher, O. Guehne, W. Duer, and R. Blatt, "Scalable multiparticle entanglement of trapped ions," *Nature*, vol. 438, p. 643, 2005.

[77] C. W. Helstrom, *Quantum Detection and Estimation Theory*. Academic Press, New York, 1976.

[78] S. L. Braunstein and C. M. Caves, "Statistical distance and the geometry of quantum states," *Phys. Rev. Lett.*, vol. 72, p. 3439, 1994.

[79] L. Pezzé and A. Smerzi, "Quantum theory of phase estimation," in *"Atom Interferometry"* (G. Tino and M. Kasevich, eds.), Proceedings of the International School of Physics "Enrico Fermi", Course 188, Varenna, p. 691, IOS Press, Amsterdam, 2014.

[80] P. Hyllus, W. Laskowski, R. Krischek, C. Schwemmer, W. Wieczorek, H. Weinfurter, L. Pezzé, and A. Smerzi, "Fisher information and multiparticle entanglement," *Phys. Rev. A*, vol. 85, p. 022321, Feb 2012.

[81] G. Tóth, "Multipartite entanglement and high precision metrology," *Phys. Rev. A*, vol. 85, p. 022322, 2012.

[82] M. Kac, "Can one hear the shape of a drum?," *Am. Math. Monthly*, vol. 73, p. 1, 1966.

[83] A. L. Burin, "Energy delocalization in strongly disordered systems induced by the long-range many-body interaction," *arXiv:cond-mat/0611387*, 2006.